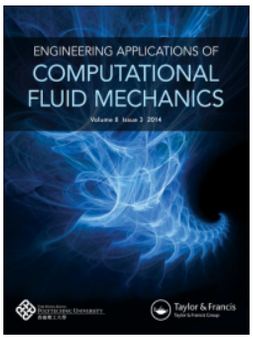

Engineering Applications of Computational Fluid Mechanics

ISSN: (Print) (Online) Journal homepage: www.tandfonline.com/journals/tcfm20

Effect of jet flow control in front of the leading bogie on the aerodynamic drag and underbody slipstream of high-speed trains

Sha Huang, Zhi-Wei Li, Wen-Jing Peng, Jin-Rong Lin, Zun-Di Huang & Guang-Zhi Zeng

To cite this article: Sha Huang, Zhi-Wei Li, Wen-Jing Peng, Jin-Rong Lin, Zun-Di Huang & Guang-Zhi Zeng (2025) Effect of jet flow control in front of the leading bogie on the aerodynamic drag and underbody slipstream of high-speed trains, Engineering Applications of Computational Fluid Mechanics, 19:1, 2447391, DOI: 10.1080/19942060.2024.2447391

To link to this article: https://doi.org/10.1080/19942060.2024.2447391

Published online: 16 Jan 2025.

ENGINEERING APPLICATIONS OF COMPUTATIONAL FLUID MECHANICS
2025, VOL. 19, NO. 1, 2447391
https://doi.org/10.1080/19942060.2024.2447391

Effect of jet flow control in front of the leading bogie on the aerodynamic drag and underbody slipstream of high-speed trains

Sha Huang[a,b], Zhi-Wei Li[a,b], Wen-Jing Peng[a], Jin-Rong Lin[a], Zun-Di Huang[a,b] and Guang-Zhi Zeng[c]

[a]School of Rail Transportation, Wuyi University, Jiangmen, People's Republic of China; [b]Jiangmen Key Laboratory of Intelligent Operation, Maintenance and Emergency Management for Rail Transit, Jiangmen, People's Republic of China; [c]Department of Civil and Environmental Engineering, The Hong Kong Polytechnic University, Kowloon, People's Republic of China

ABSTRACT

Bogies are significant contributors to the aerodynamic resistance of high-speed trains, making them key areas of consideration for flow control and optimization. This study applied an air jet slot positioned in front of the leading bogie to explore its effectiveness in reducing the train's aerodynamic resistance under Reynolds number (*Re*) of 2.64×10^6. The *SST k-ω*-based Improved Delayed Detached Eddy Simulation (IDDES) turbulence model was utilized to study the effects of various jet velocities and angles on the transient and time-averaged flow change underneath the train, as well as their correlations with aerodynamic drag reduction rates (δ). Results indicate that the δ exhibits a notable upward trajectory with increasing jet velocity, followed by a slight decline once the jet velocity exceeds 0.8*U* (the train speed) at jet angles below 75°. Moreover, the increase of jet velocity results in a significant decrease in slipstream velocities but an increase in turbulent vorticity, intensity and kinetic energy underneath the leading bogie after the jet slot. The impact of jet angle is comparatively less pronounced than that of jet velocity, the disparity in drag reduction rates caused by varying jet angles remains within a range of 2.4% at a specific jet velocity, and the mean slipstreams and turbulent variables demonstrate minimal changes with varying jet angles. Optimal aerodynamic drag reduction is achieved with an air jet velocity of 0.8*U* and an angle of 15°, which is 6.43% for the whole train. The results presented in this paper suggest a new aerodynamic drag reduction method based on active flow control, providing engineering implications for the energy-efficient development of high-speed trains.

ARTICLE HISTORY
Received 21 July 2024
Accepted 21 December 2024

KEYWORDS
High-speed trains; bogies; jet flow control; aerodynamic drag; slipstream

1. Introduction

Advancements in train speeds have increased aerodynamic drag and noise, causing higher energy consumption and environmental pollution. These challenges greatly hinder the further speed increase and sustainable development of high-speed trains (HSTs) (Muñoz-Paniagua & García, 2020). As a crucial element that affects the train's operation safety and stability, the bogie possesses complicated structures that generate violent flow separations and interactions. These flow phenomena significantly contribute to aerodynamic resistance and noise generation (Jönsson et al., 2014; Thompson et al., 2015; Wang et al., 2018; Zhu & Hu, 2017). Therefore, the bogie region has become a key consideration area for flow control and optimization.

In recent years, numerous scholars have endeavoured to enhance the aerodynamic efficiency of trains through optimization of bogie region configurations. Gao et al. (2019) discovered that positions of bogies significantly affect the underbody flow of the train, rearward relocation of the bogie was found to be an effective strategy for reducing aerodynamic drag. Zhang, Wang, et al. (2018) investigated the impact of the bogie's cut-outs angle on the wake flow and proposed a novel compound bogie cut-outs design, achieving a 2.92% reduction in aerodynamic drag for a train consisting of three coaches. Wang et al. (2019) achieved a 12.5% reduction in drag by implementing full-size bogie fairings. The effectiveness of bogie fairings and enclosed bottom plates has also been confirmed by (Deng et al., 2024). Furthermore, Wang et al. (2020) revealed that Jacob's bogies successfully mitigated the slipstream velocity adjacent to the track and decreased the aerodynamic drag by 10%, exhibiting commendable efficacy in improving trackside safety. Dai et al. (2024) applied shields beneath bogies and got a considerable aerodynamic reduction of 37.7%. Liu et al. (2024) designed a wedge-shaped deflector at the bottom of the frontal bogie, in conjunction with

CONTACT Zhi-Wei Li lzhw1205@163.com School of Rail Transportation, Wuyi University, Jiangmen 529020, China

an optimized streamlined shape, a notable decrease of 5.87% in the aerodynamic drag was obtained. Zhang et al. (2023a) applied diversion slots near the bogie cavities of the HST. The diversion slots deflected the airflow from entering the bogie regions, reaching a maximum reduction of 9.4% in the aerodynamic drag of the tail. Some scholars have explored the application of vortex generators in various regions of trains for purposes of flow control and aerodynamic drag reduction (Du et al., 2022; Li et al., 2023; Zhang et al., 2023b, 2024).

The active flow control method has been proven to be another effective way of optimizing the aerodynamics of moving objects. Yousefi et al. (2014b, 2014a, 2015) applied tangential/perpendicular sucking or blowing on a NACA 0012 airfoil, effects of the jet locations, widths and lengths on the aerodynamic performance of the airfoil were evaluated. Findings in these studies indicated that tangential blowing at the trailing edge with larger jet widths and centre sucking at the leading edge of the wing's upper surface with longer jet lengths (greater than half the wingspan) was effective in increasing the lift-to-drag ratio of the airfoil. Wang et al. (2022) also experimentally studied the effects of blowing and suction jets on the aerodynamic characteristics of a NACA0012 airfoil, and got the best performance in lift with a single blowing jet located 0.2 times the chord length from the leading edge. Guo et al. (2023) confirmed that air blowing at the base of a flat plate with a blunt trailing edge effectively decreased the turbulent kinetic energy in the near-wake region, and successfully reduced both the amplitude and bandwidth of aerodynamic noise. Currently, scholars have attempted to employ active flow control techniques to optimize the HST's aerodynamic performance. Chen et al. (2023) reduced the aerodynamic drag by 10.78% through implementing air-blowing slots on the streamlined head and tail noses of a three-coach train. Che et al. (2023b) applied air-blowing/sucking holes on the rear coach and got a reduction of 8.69% in aerodynamic drag and 30.4% in lift for the tail car. Che et al. (2023a) also implemented air-blowing slot in the side transition region of the streamlined tail and got a drag reduction of 6.53% for a maglev train with three cars. Similarly, Cui et al. (2023) employed a combined air suction-blowing approach at the rear of a 400 km/h EMU and found that sucking on the upper separation region and blowing on the bottom nose region significantly mitigated the pressure drag experienced by the tail car. Mitsumoji et al. (2014) effectively mitigated the aerodynamic noise of pantographs through the utilization of a plasma actuator, and Huang et al. (2024) introduced an air jet in front of pantographs to successfully reduce the aerodynamic drag of pantographs. Additionally, the active flow control strategy was applied to improve the safety of trains when encountering strong crosswind conditions (Chen et al., 2022; Chen et al., 2024; Li et al., 2018).

Previous studies have been dedicated to developing passive flow control methods such as fairings and shields around bogies to optimize the aerodynamic performance of HSTs. Although full-size fairing measures could achieve a significant reduction in aerodynamic resistance, they are not conducive to heat dissipation and ventilation in bogie areas. Furthermore, the spatial constraints in the bogie region limit the potential of significant advancements in large-scale shape optimizations and extra deflector installations, posing challenges to innovative breakthroughs. Experimental and numerical studies have proved that air-blowing/sucking technology has significant potential in controlling and optimizing the aerodynamics both for ground vehicles and air vehicles. However, this method has not yet been applied in the bogie area. Some scholars have done some investigation in controlling the cavity flow by active method, e.g. Choi and Lee (2023) applied a transverse slot in the upstream region of the cavity leading edge, decreasing the pressure fluctuation on the cavity wall. Melih et al. (2023) also numerically studied the effects of active mass flow injecting on the aerodynamic performance of an M219 cavity, effectiveness of flow optimization and noise suppression were verified. These studies inspired us to conduct investigations on applications of air blowing in front of the bogie cavity.

Aiming to optimize the flow behaviour in the bogie region and mitigate the aerodynamic forces encountered by trains, this paper proposed an active flow control approach by applying a jet slot positioned in front of the leading bogie, effects of various jet velocities, angles on the aerodynamic drag coefficient, as well as variation in field velocities and surface pressures were investigated numerically. The paper begins with an introduction of the numerical model in Section 2, grid refinement analysis and experimental validation are conducted for the uncontrolled case before comprehensive simulations with varying control parameters. The aerodynamic drag and underbody slipstream of the HST under different jet velocities and angles are analyzed in Sections 3 and 4. Conclusions and future studies are discussed in section 5. The outcomes are expected to make a valuable contribution to the energy conservation and sustainable development of HSTs.

2. Methodology

2.1. Geometries

The study utilized a typical HST model of the CRH (China Railway High-speed) series consisting of three

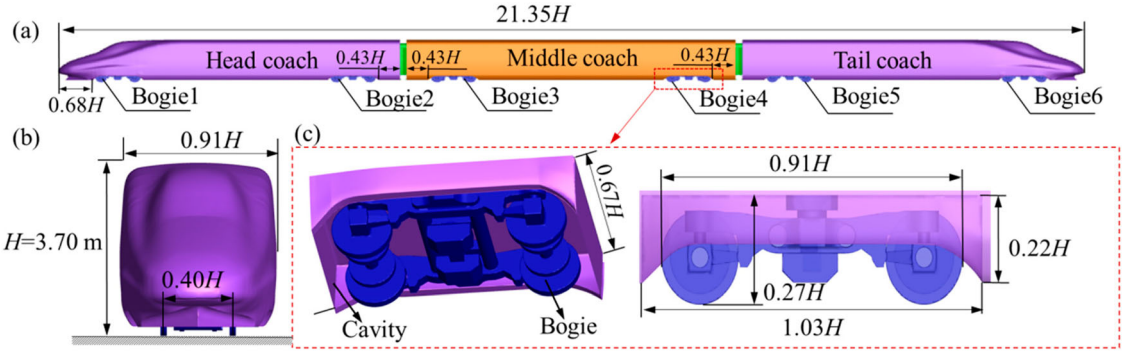

Figure 1. Geometry and dimension of the train model.

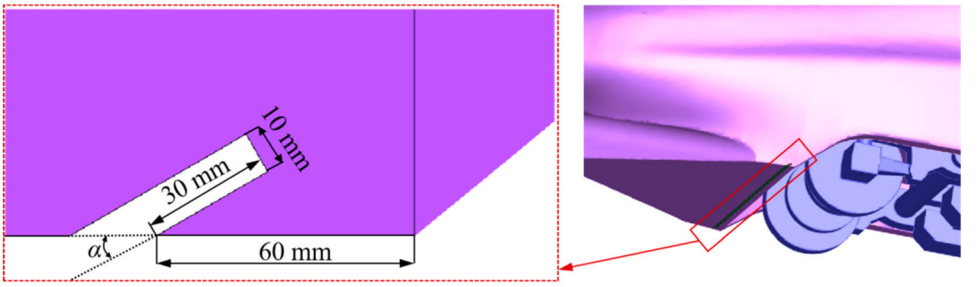

Figure 2. Positions and dimensions of jet slots in front of the leading bogie.

coaches with intricate bogie structures, as indicated in Figure 1(a) and (b). Dimensions of the train include a height (H) of 3.70 m, a width of 0.91H, and a total length of 21.35H. Bogies are located in rectangular cavities, detailed dimensions and locations of bogies and cavities are provided in Figure 1(a–c).

According to statistics, the bogie region accounts for 27.4% of the overall aerodynamic resistance in an eight-car HST, with the leading bogie exhibiting significantly higher resistance compared to the remaining bogies (Yao et al., 2012). Therefore, the jet slot was positioned in front of the leading bogie at a distance of 60 mm from the frontal plate of the cavity, with a fixed height of 30 mm and width of 10 mm, as depicted in Figure 2. Effects of various jet velocities (V_{jet}), and jet angles (α) on the flow behaviour and aerodynamic drag of trains were investigated.

The Finite Volume Method (FVM) is commonly employed for CFD calculations (Aultman et al., 2022). As shown in Figure 3, to simulate the infinite space surrounding the train using a limited domain, a cuboid (Domain 1) with dimensions of 32H and 16H in width and height, respectively, was established. The train was displaced at the spanwise centre of the cuboid with a distance of 27H from the domain entrance, leaving a sufficient downstream distance (approximately 60H) to the exit to ensure full development of the wake flow. Although the dimensions of the cuboid were selected to satisfy the requirement outlined in the CEN European Standard (2013) and Chinese TB Standard (China National Railway Administration, 2018), a larger domain (Domain 2) with upstream distance extended to 42H (approximately 6 times the length of a coach) and the downstream distance extended to 112H (approximately 16 times the length of a coach) was also conducted to verify the adequacy of the domain length. A velocity-inlet boundary condition was imposed on the entrance with a uniform velocity equivalent to the speed of the train (U), while the opposite exit was specified as a pressure outlet. The lateral and upper boundaries were defined as symmetry planes (Chen et al., 2023; Guo et al., 2024; Li et al., 2021; Liang et al., 2020; Muñoz-Paniagua & García, 2020), whereas lower surface was designated as a slipping wall with velocity consistent with the velocity inlet.

2.2. Grid strategy

The computational domain was discretized using the trimmed mesh technology implemented in Star-CCM + software, which predominantly employed hexahedral grids to minimize grid quantities and mitigate numerical diffusion, this mesh strategy is widely used in the CFD simulation of HSTs (Bao et al., 2020; Li et al., 2019; Meng et al., 2021). To precisely simulate the flow variations in the boundary layer, 15 layers of prism grids with an overall thickness of 0.05 m growing at a rate of

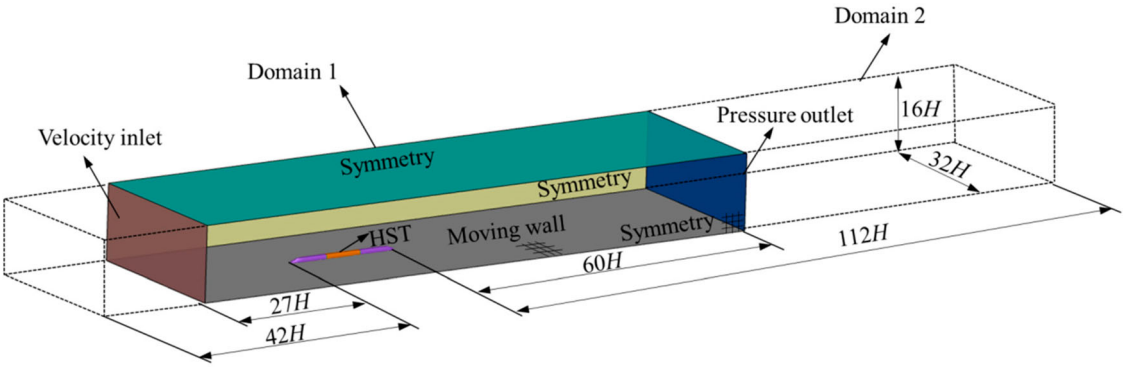

Figure 3. Computational domain.

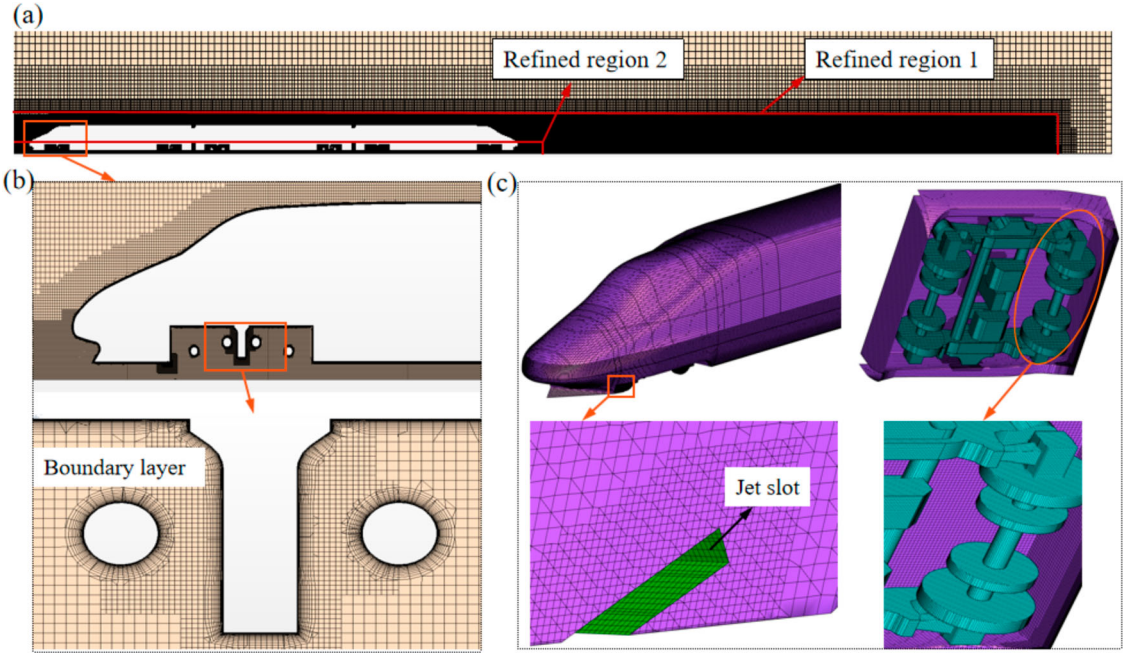

Figure 4. Computational grids for the medium mesh: (a) in a central vertical plane; (b) around the train head and boundary layer; (c) around the bogie and jet slot.

1.2 were created around the vehicle surface, as shown in Figure 4(b). Figure 4(c) demonstrates the refined surface grid of the HST, with particular attention given to the grid around the bogie and near the jet slot. Furthermore, two refined spatial regions were constructed, as depicted in Figure 4(a), Refined region 1 located 2.7 H from the train nose and extended approximately 42 H towards the far end to capture the transient flow variations near the train and in the wake. Refined region 2 was established along the entire bottom section of the train to accurately simulate the underbody flow change, detailed dimensions and mesh resolutions were listed in Table 1 and 2.

Grid is a crucial factor affecting the accuracy and efficiency of numerical calculations. In this study, three sets of girds with increasing grid numbers of 18, 38, and 70 million were built for Domain 1, the maximum and averaged dimensionless wall distances in the streamwise direction (l^+), spanwise direction (s^+), and wall-normal direction (y^+), were listed in Table 1. These three parameters were defined by the following Equations. As indicated in Table 1, the wall-normal distances

Table 1. Grid resolutions in boundary layers.

Mesh	Number ($\times 10^6$)	y^+_{max}	y^+_{min}	l^+_{max}	l^+_{mean}	s^+_{max}	s^+_{mean}
Coarse	18	2.8	1.2	560	240	560	240
Medium	38	2.8	1.2	280	120	280	120
Fine	70	2.8	1.2	140	60	140	60

Table 2. Grid resolutions in refined regions.

Mesh	Refined region 1		Refined region 2	
	Dimension	Mesh size	Dimension	Mesh size
Coarse	Length: 42 H	0.04 H	Length:22H	0.02 H
Medium	With: 2 H	0.04 H	With: H	0.01 H
Fine	Height: 1.5 H	0.02 H	Height:0.34H	0.01 H

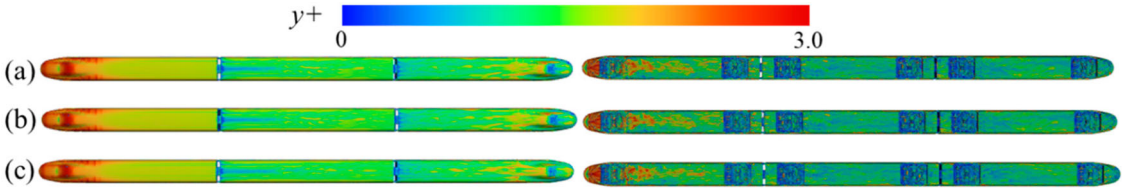

Figure 5. Contours of $y+$ on the train surface: (a) coarse mesh; (b) medium mesh; (c) fine mesh.

remain the same for the three meshes, grids are refined in the streamwise and spanwise direction with constant factor of 2. The maximum value of y^+ all over the train surface was smaller than 3, with an average value of around 1 for all three meshes, meeting the boundary layer grid requirement of IDDES turbulent model. Contours of $y+$ on the train model surface are displayed in Figure 5, the majority of regions have $y+$ around 1, except for relatively larger values appearing in the streamlined head region.

$$l^+ = \Delta l \mu_\tau / \upsilon \tag{1}$$

$$y^+ = \Delta n \mu_\tau / \upsilon \tag{2}$$

$$s^+ = \Delta s \mu_\tau / \upsilon \tag{3}$$

where Δl, Δs represents the cell width in the streamwise and spanwise direction, respectively, and Δn is the distance from the first nodes to the train surface in the wall-normal direction; μ_τ is the friction velocity, and υ is the air kinematic viscosity.

2.3. Validation

2.3.1. Results convergence

To verify the convergence of the transient results, time histories of flow field variables including the streamwise flow velocity (V_x/U) and turbulent kinetic energy (TKE) at a spatial point are demonstrated in Figure 6(a) and (b). The spatial point is located $0.5H$ from the centre of the track (COT) and $0.5H$ from top of rail (TOR) at the centre of the train length, which is approximately $0.05H$ away from the train surface. Besides, time histories of wall shear stress on the train surface, as well as the aerodynamic drag coefficient (C_d) of the head coach, are given in Figure 6(c) and (d). C_d is defined as $C_d = F_d/0.5\rho U^2 S$, where F_d is the aerodynamic drag force and ρ denotes the air density at 15°C; U is the train's operational speed and S represents the cross-sectional area of the train. As indicated in Figure 6, all aerodynamic variables periodically fluctuate around a stable averaged value, the calculation results are considered converged and ready for data-sampling post processing and analyzing.

2.3.2. Grid refinement study and discretization error analysis

In the grid convergence study, the order of accuracy (p), which involves the behaviour of the solution error, is usually considered and calculated by Equation (4). Since the relative error (e_a) does not consider the order of convergence, it may lead to an underestimation or overestimation of the error, extrapolated error (e_{ext}) and grid convergence index (GCI) are also calculated through Equation (5) and (6), details can be found in reference (Celik et al., 2008).

$$p = \frac{1}{ln(r)} |ln|\varepsilon_{32}/\varepsilon_{21}|| \tag{4}$$

where r is the grid refinement factor, $r = 2$ is used for the three grids in this paper. $\varepsilon_{32} = \varphi_3 - \varphi_2$, $\varepsilon_{21} = \varphi_2 - \varphi_1$ and φ_k denotes the numerical results on the k^{th} grid, $k = 1, 2, 3$ in this paper represent the three grids with increasing relative grid size, namely fine, medium and coarse meshes, respectively.

$$e_{ext}^{21} = |(\varphi_{ext}^{21} - \varphi_1)/\varphi_{ext}^{21}| \tag{5}$$

$$GCI_{21} = (F_S e_a^{21})/(r^p - 1) \tag{6}$$

$$\varphi_{ext}^{21} = (r^p \varphi_1 - \varphi_2)/(r^p - 1) \tag{7}$$

$$e_a^{21} = |(\varphi_1 - \varphi_2)/(\varphi_1)| \tag{8}$$

In Equation (5), the extrapolated results φ_{ext}^{21} can be calculated through Equation (7). In equation (6), $F_s = 1.25$ is a factor of safety for comparison over three grids, and e_a represents the relative error, defined in equation (8).

In grid refinement analysis, the mean normalized slipstream velocities ($\overline{V_x}/U$) measured at a distance $0.5H$ from the COT and $0.5H$ from the TOR are compared between different meshes and showed in Figure 7(a), x and L in the x-axis represent the distance from the head nose and total length of the train, respectively. According to Celik et al. (2008), the local order of accuracy p calculated from equation (4) ranges from 0.40–4.13, with a global average value (p_{ave}) of 2.07, which agrees well with the formal second-order solution scheme in the calculation. Among these 20 points, 35% exhibit

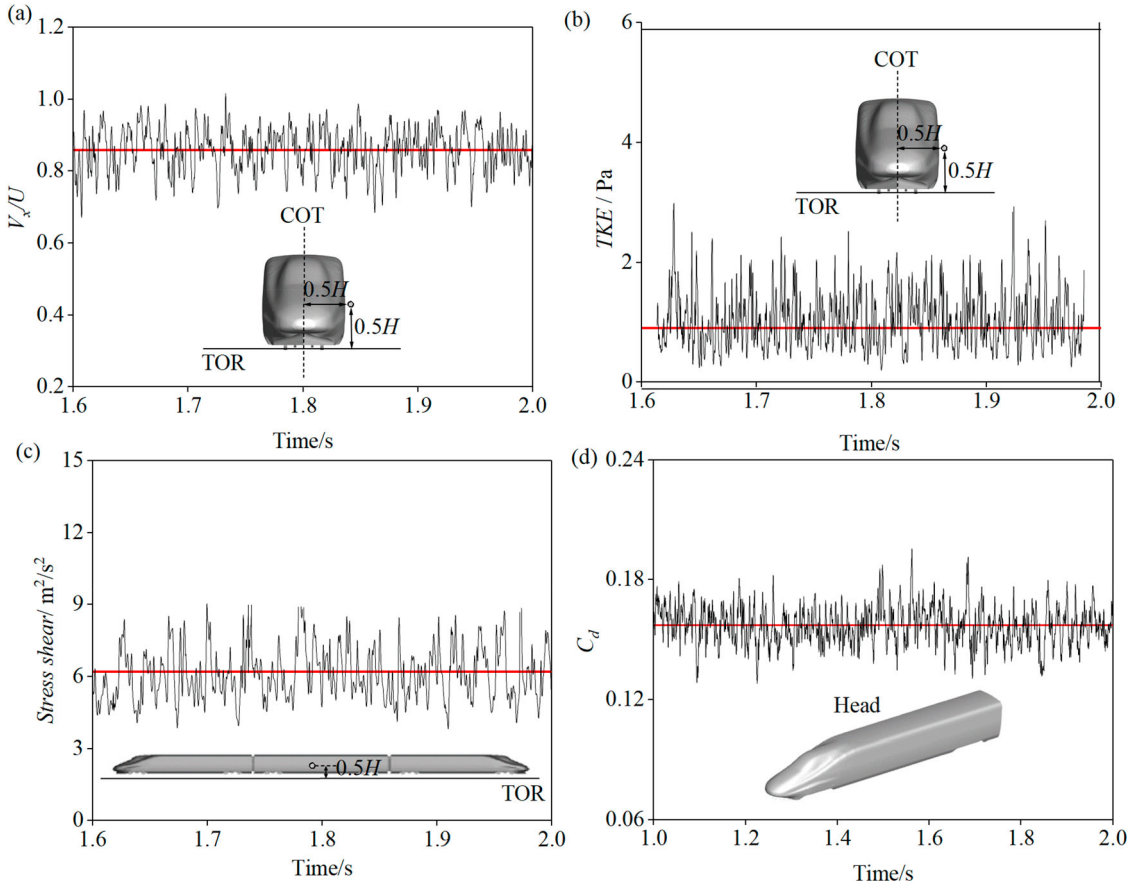

Figure 6. Time histories of aerodynamic variables around and on the train model: (a) streamwise flow velocity near the train; (b) turbulent kinetic energy near the train; (c) shear stress on the train surface; (d) aerodynamic drag of the head coach.

oscillatory convergence. The calculated relative errors and extrapolated relative errors are shown in Figure 7(b) and (c), and the extrapolated mean velocity profile with discretization error bars (GCI) is displayed in Figure 7(d). As indicated in Table 3, the relative and extrapolated relative errors for the fine and medium meshes are within 1.2% and 2.8%, 2.1% and 2.9%, respectively. The extrapolated values for the fine mesh fit well with the medium mesh, except for larger GCI values in areas ranging from 0.4 L to 0.7 L, the maximum GCI values for the fine and medium meshes are 2.6% and 3.8%, respectively. Although the difference in discretization errors for the fine and medium meshes are not that significant, the computational cost for the fine mesh is approximately 12 times greater than that of the medium mesh. Therefore, the medium mesh strategy was chosen for the subsequent investigations in this study.

2.3.3. Domain length adequacy

The same medium mesh strategy and solver setting were adopted for the larger domain case. To evaluate the influence of the upstream distance on the incoming flow in front of the train head, time-averaged streamwise velocity distributed along two vertical lines at distance 0.5H and 0.1H from the front nose of the train head are displayed in Figure 8. Velocity distributions from two domains agree well with each other, as the height exceeds 2 times the height of the train, field velocity remain consistent with the incoming flow. By locally refining the data in the bottom region ($h/H \leq 2$) where velocities change severely, the disparity between the twin domains is very minor, with the greatest differences being only 1.03% at $X = -0.5H$ and 0.33% at $X = -0.1H$, which validates the adequacy of the upstream distance of 27H for fully development of the incoming flow. Additionally, wake structures, characterized by Q (the second invariant of velocity gradient) and coloured by the streamwise velocity, are compared in Figure 9, it shows that the developed wake length is almost identical for the two domain lengths (*L1* for Domain 1 with a downstream distance of 60H and *L2* for Domain 2 with a downstream distance of 112H). All these comparisons comprehensively verify the adequacy of upstream and downstream distance of Domain 1 to ensure full development of the incoming and wake flow.

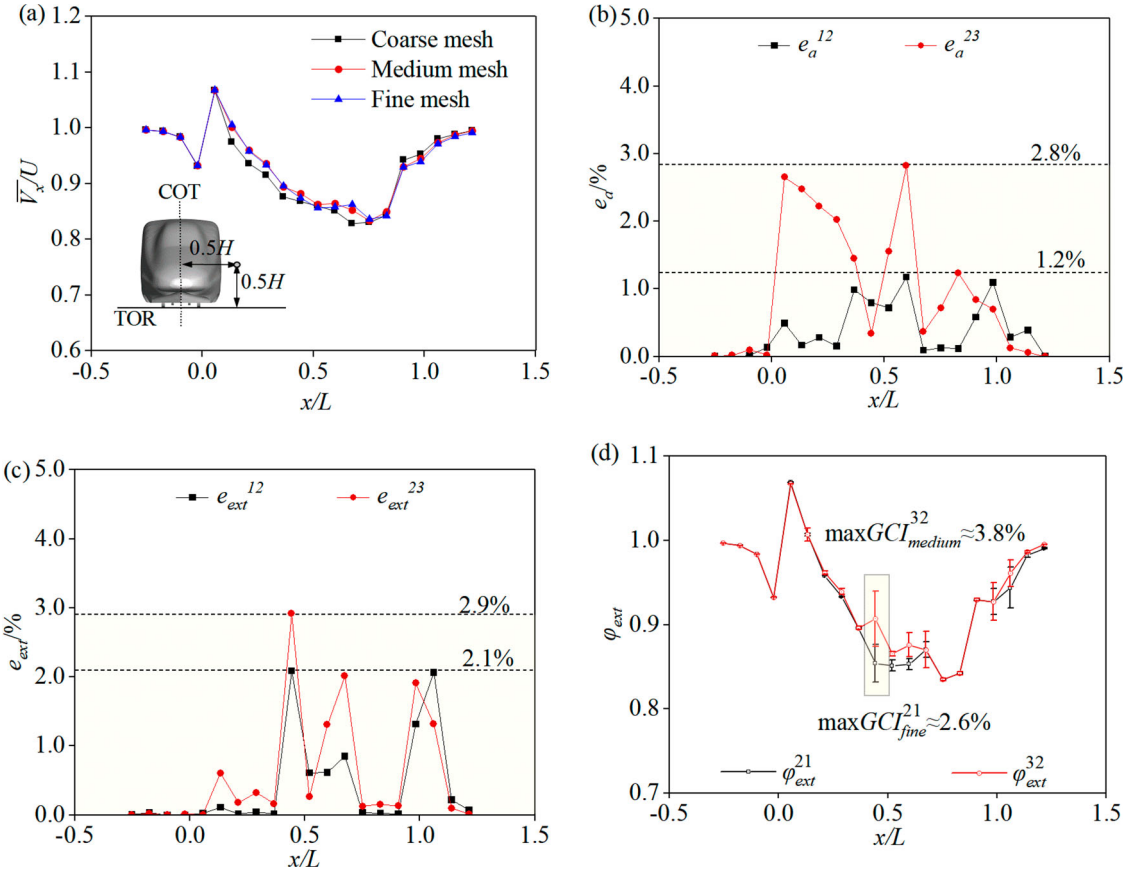

Figure 7. Result comparisons between different meshes and discretization errors: (a) mean velocity profile; (b) relative error; (c) extrapolated relative error; (d) extrapolated mean velocity profile and GCI errors based on local *p*.

Table 3. Maximum errors between three meshes.

Mesh	e_{a-max} %	$E_{ext-max}$ %	GCI_{max} %	Computational cost (Core·h)
Fine [21]	1.2	2.1	2.6	17920
Medium [32]	2.8	2.9	3.8	222400

2.3.4. Numerical algorithm validation

In this study, the commercial CFD software Ansys Fluent was used for numerical simulations (Ansys Fluent, 2019). The operating speed of the HST (U) was determined to be 300 km/h, equivalent to a Mach number of 0.245, which is below 0.3, thus an incompressible transient solver was employed. In additional, to meet the boundary layer resolution requirement, the computational model was 1/8 scaled to ensure that the dimensionless wall distance of the first layer ($y+$) was less than 1. Under this circumstances, the Re was calculated to be 2.64×10^6, greatly surpassing the critical Re of 2.5×10^5 required for reduced-scale model test (CEN European Standard (2013)) and 3.6×10^5 required for flow self-simulation (Che et al., 2023a; Huang et al., 2016). The *SST k-ω* based IDDES hybrid turbulence model was employed in this study. Although Large Eddy Simulation (LES) is acknowledged as the most accurate method for simulating the turbulent characteristics of moving objects. These stringent gird requirements lead to substantial computational costs, thus the LES model is generally applicable only to smaller and simpler geometries. The IDDES model is a hybrid RANS-LES approach that strikes a balance between computational efficiency and accuracy, particularly suitable for complex flow simulations with limited computational resources. This method has been successfully employed in simulating the transient aerodynamics of trains (Dong et al., 2020; Niu et al., 2020; Xiao et al., 2020).

The model combines the advantages of wall-modelled LES (WMLES) and the delayed detached eddy simulation (DDES). It introduces a blending function, defined as $\tilde{f}_d$ in Equation (9), to the length scale formulation of the DDES model to realize an automatic determination between WMLES and DDES modes, more details about the governing equations can be found in (Shur et al., 2008) and (Gritskevich et al., 2012).

$$\tilde{f}_d = max\{(1 - f_d), f_B\} \tag{9}$$

$$f_B = min\{2\exp(-9\alpha^2), 1.0\} \tag{10}$$

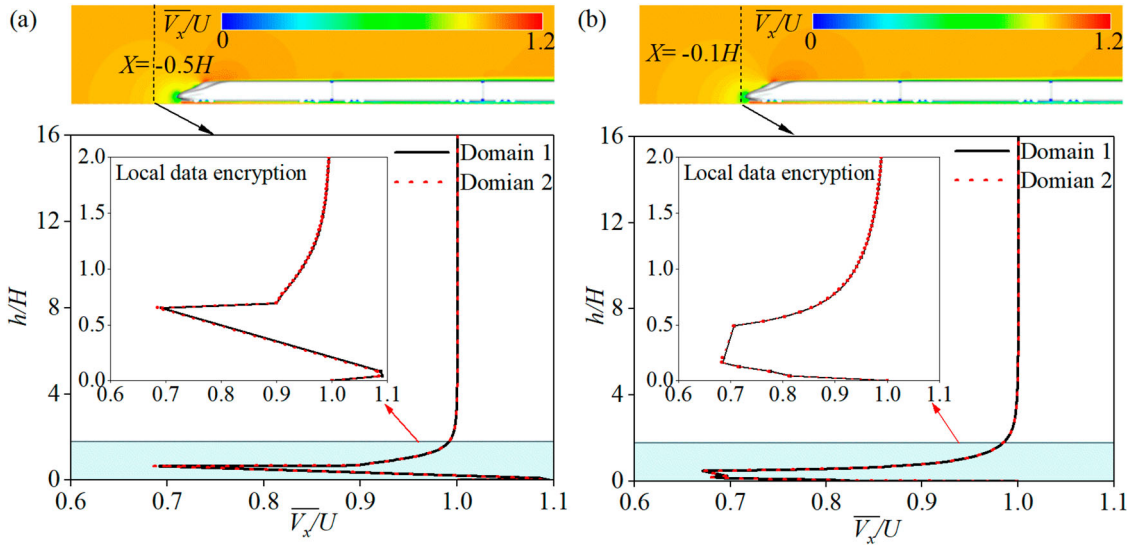

Figure 8. Time-averaged flow velocity along two vertical lines in front of the train head nose: (a) $X = -0.5H$; (B) $X = -0.1H$.

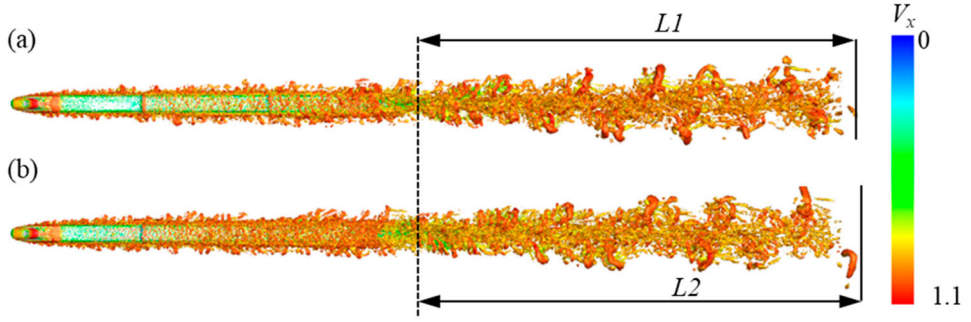

Figure 9. Iso-surface of $Q = 2000$ in the train wake under different domain lengths: (a) Domain 1; (b) Domain 2.

$$f_d = 1 - tanh(8r_d)^3 \tag{11}$$

with $\alpha = 0.25 - d_w/h_{max}$, while $h_{max} = max\{h_x, h_y, h_z\}$ is the maximum locale grid spacing and d_w is the distance to the wall. r_d is borrowed from the SA RANS model, which can be found from (Sparlart & Allmaras, 1992).

The length scale of the IDDES can be defined as:

$$l_{IDDES} = \tilde{f}_d(1 + f_e)l_{SST} + (1 - \tilde{f}_d)l_{LES} \tag{12}$$

where

$$f_e = max\{(f_{e1} - 1), 0\}\psi f_{e2} \tag{13}$$

in which

$$f_{e1}(d_w/h_{max}) = \begin{cases} 2\exp(-11.09\alpha^2) & if\alpha \geq 0 \\ 2\exp(-9.0\alpha^2) & if\alpha < 0 \end{cases} \tag{14}$$

$$f_{e2} = 1.0 - \max\{f_t, f_l\} \tag{15}$$

$$f_t = tanh[(c_t{}^2 r_{dt})^3] \tag{16}$$

$$f_l = tanh[(c_l{}^2 r_{dl})^{10}] \tag{17}$$

where r_{dt} and r_{dl} are turbulent and laminar analogues of r_d, c_t and c_l are model constants depending on the RANS model and should be readjusted to ensure that f_{e2} is zero when either r_{dt} or r_{dl} is close to 1.0.

Based on the above covering equations, it can be concluded that when $r_{dt} \ll 1$, $\tilde{f}_d$ is equal to f_B, the calculation automatically switch to WMLES mode. Otherwise, DDES mode is activated.

The gradient was resolved using a Least Squares Cell-based method, pressure was discretized utilizing a Second Order scheme, and the QUICK format was applied for moment and turbulent discretizations. The transient time step was set as 5×10^{-5}, based on what the convective Courant number around the train model was calculated as less than 1, as indicated in Figure 10. The transient calculation duration of 2s was set, corresponding to 3 flow passages of the calculation domain and 16 flow passages of the train model, the calculation time for the longer domain case was correspondingly extended. The number of iterations per step may affect the result convergence and accuracy. To assess this, a limited convergence study using 25, 50 and 100 iterations per step

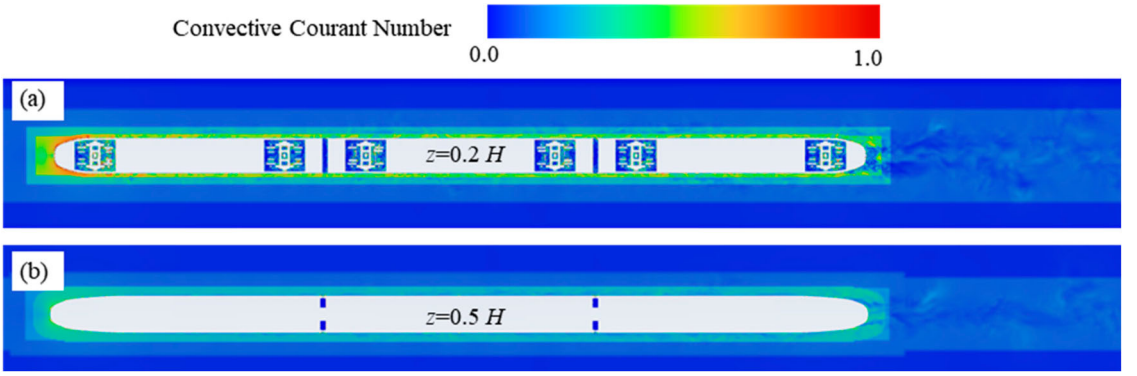

Figure 10. Convective Courant number around the train: (a) plane $z = 0.2\,H$; (b) plane $z = 0.5\,H$.

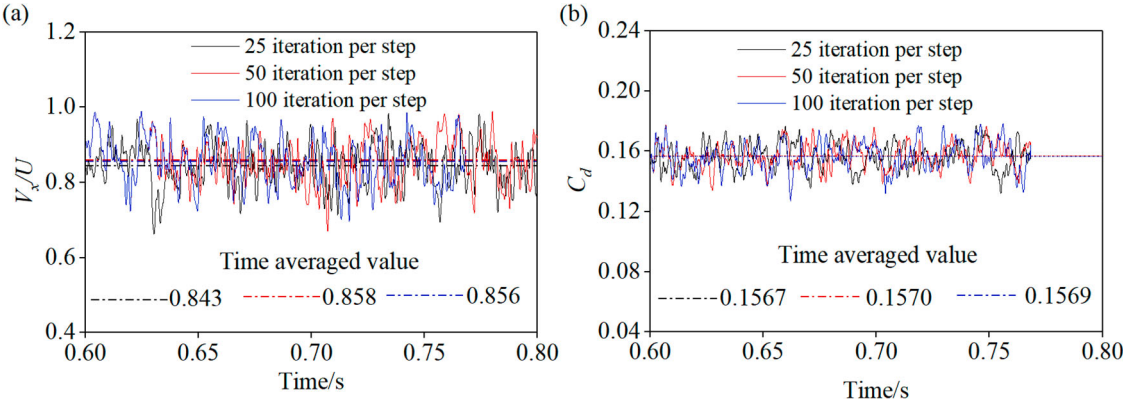

Figure 11. Time histories of aerodynamic variables under different iteration numbers per step: (a) streamwise velocity; (b) aerodynamics drag of the head coach.

Table 4. Residual magnitude under different iteration numbers.

Iteration numbers per strep	*continuity*	V_x	V_y	V_z	k	ω
25	10^{-4}	10^{-8}	10^{-9}	10^{-9}	10^{-6}	10^{-7}
50	10^{-5}	10^{-8}	10^{-9}	10^{-9}	10^{-6}	10^{-7}
100	10^{-5}	10^{-8}	10^{-9}	10^{-9}	10^{-6}	10^{-7}

over a partial transient simulation period was carried out. As indicated in Figure 11, time histories of the streamwise velocity at a point located $0.5H$ from the COT and $0.5H$ from the TOR at the centre of the train length, as well as the aerodynamic drag of the head coach, are compared between different iteration numbers. The data exhibit fluctuations around an averaged value, and the differences in the time-averaged C_d values for the three iteration numbers are not statistically significant. However, less iteration number of 25 leads to a relatively smaller time-averaged field velocity compared to an iteration number of 50. The time-averaged field velocity obtained from an iteration number of 100 closely approximates that of 50 iterations, with difference of only 0.2%. Additionally, the residual comparisons presented in Table 4 demonstrate that the residual magnitudes for the velocity, k and ω terms remain consistent under the three iteration numbers. However, an iteration number of 25 only reduces the continuity residual to 10^{-4}, whereas iteration numbers of 50 and 100 reduce the continuity residual to 1.2×10^{-5}. In summary, as the number of iterations per step exceeds 50, transient and time-averaged results change little with increasing iteration numbers, confirming the convergence and accuracy of the results. Considering that a larger number of iterations per step results in significant computational costs, an iteration number of 50 per strep was chosen for calculations in this study.

To validate the numerical algorithm, results from the IDDES calculation were compared with the wind tunnel test conducted by Zhang et al. (2018). This experiment was carried out in an $8 \times 6\,m^2$ wind tunnel, a 1/8 scaled three-coach CRH2 HST model was located on a supporting plate with streamlined designed leading and trailing edges, the plate was located 1.06 m from the tunnel floor to eliminate the ground boundary layer effect. A corresponding numerical model with an extended rear end was established to match the wind tunnel test, as indicated in Figure 12(a). Figure 12(b–d)

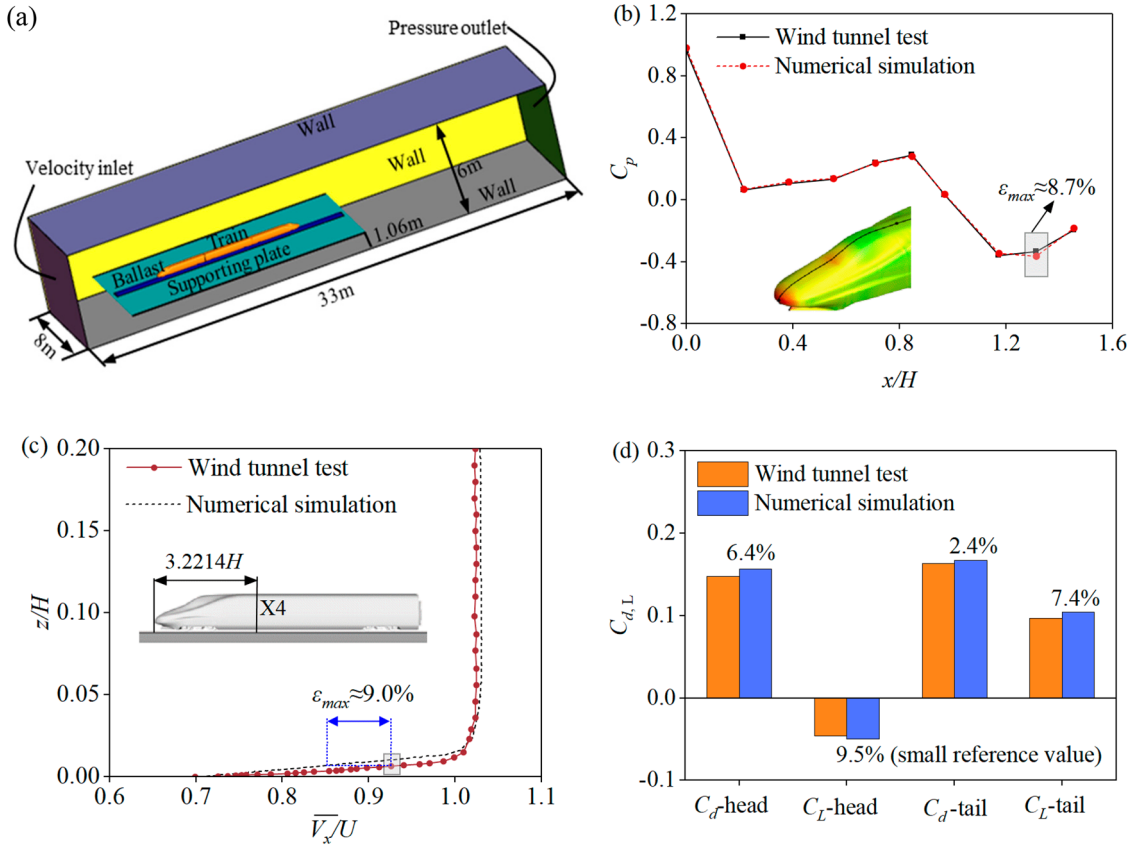

Figure 12. Comparisons between numerical simulation and wind tunnel test: (a) corresponding numerical model; (b) pressure coefficient; (c) velocity distribution in boundary layer; (d) aerodynamic drag and lift.

compares the numerical and wind tunnel results for various aerodynamics variables, including the surface pressure coefficient (C_p) along the longitudinal centre of the streamlined head, mean velocity ($\overline{V_x}/U$) in the boundary layer at position *X4*, and aerodynamic drag and lift coefficient (C_L) of the train model. C_p and C_L are defined in Equations (18)∼(19). The numerical C_p curve fits well with the wind tunnel results, with a maximum discrepancy of 8.7% observed in the transition area. The numerical velocity profile also closely matches the wind tunnel data, except for slightly lower values near the train surface, with a maximum error of approximately 9.0%. The largest difference in aerodynamic drag is 6.4% at the head, while aerodynamic lift shows a relatively high error of 9.5% due to its small reference value (−0.033, close to zero). These errors may stem from minor differences in geometry modelling, point locating, and other numerical factors. Despite some errors reaching 9%, they are all within the acceptable 10% limits for numerical engineering applications according to TB standard (China National Railway Administration, 2018).

$$C_P = \frac{p - p_0}{0.5\rho U^2} \tag{18}$$

$$C_L = \frac{F_L}{0.5\rho U^2 S} \tag{19}$$

where p represents the local surface pressure, and p_0 is the atmospheric pressure. U was chosen as 60 m/s in the wind tunnel test. S is 0.175 m^2 for the scaled model.

3. Results analysis

As the incoming flow traverses the head nose, it moves rapidly with an increasing velocity towards the upper and lower sections of the train. The accelerated bottom airflow interacts with the complex bogies in cavities, leading to substantial alternations in the flow field and the formation of complex vortex structures, consequently resulting in notable aerodynamic loads. To investigate the effect of jet flow control in front of the leading bogie on the underbody flow field and determine the pattern of aerodynamic drag variations on specific components, the dimensionless reduction rate of aerodynamic drag (δ) is introduced and defined in Equation (20). δ involves the aerodynamic drag reduction in each component by multiplying the proportion of aerodynamic forces contributed by

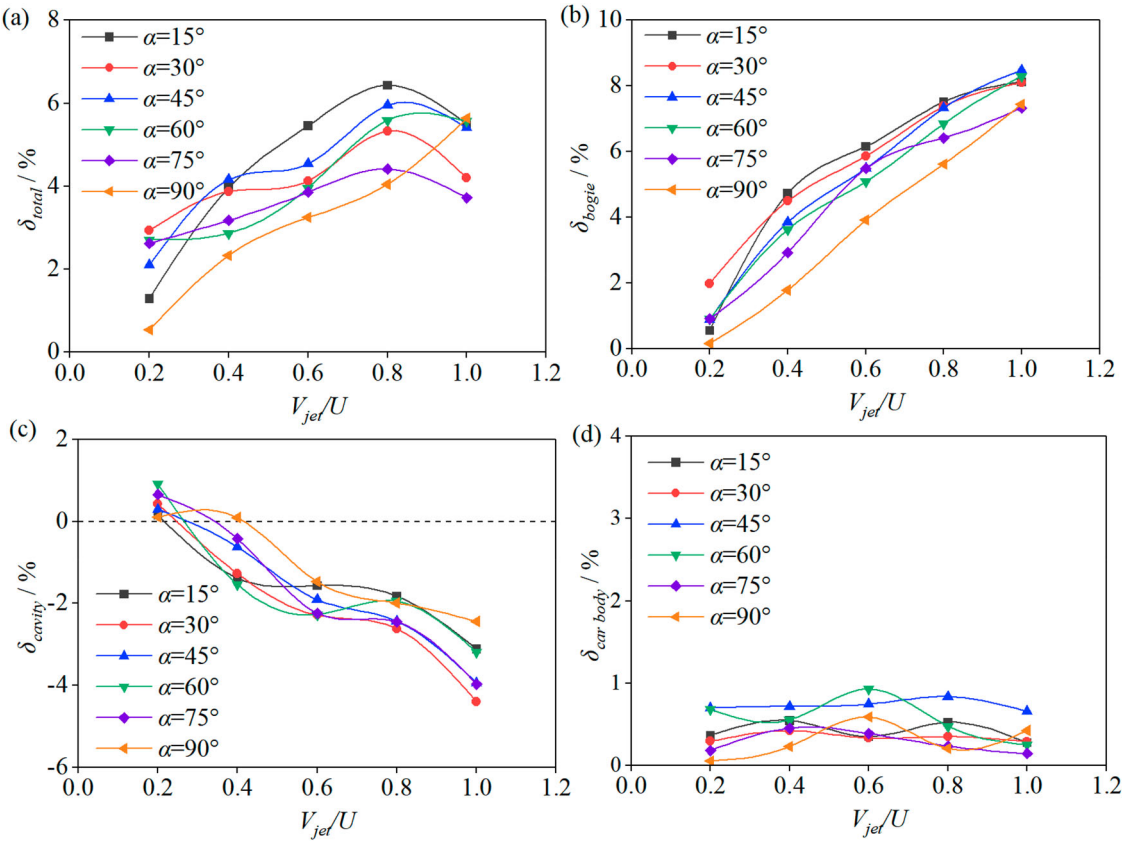

Figure 13. Reduction rates in aerodynamic drag with jet velocity at various angles for individual components of the train: (a) whole train; (b) bogie; (c) cavity, and (d) car body.

individual parts to the overall train.

$$\delta_i = \frac{F_{d0,i} - F_{d,i}}{F_{d0,i}} \times \frac{F_{d0,i}}{F_{d0,total}} \times 100\% \qquad (20)$$

where $F_{d,i}$ represents the aerodynamic drag of individual components under various jet conditions, while $F_{d0,i}$ and $F_{d0,total}$ denote the aerodynamic drag of individual components and whole vehicle for the original train without jet flow control, respectively. When the values of δ is positive, the jet flow control schemes exhibit a effective reduction in aerodynamic drag; Otherwise, the schemes only yield an enhancement effect.

3.1. Impact of air jet on the aerodynamic drag of the train

3.1.1. Effect of jet velocity

Figure 13 presents the variations in drag reduction rate δ for different components with jet velocities at varying jet angles. As shown in Figure 13(a), the overall reduction rate δ_{total} demonstrates a notable upward trajectory with increasing jet velocity until it reaches $0.8U$, after which it decreases for jet angles below 75°. However, the behaviour differs at a jet angle of 90°, as it consistently exhibits an increasing trend with jet velocity. In order to further examine the factors contributing to changes in total resistance, a comprehensive analysis of the reduction of aerodynamic drag for the bogie (δ_{bogie}), the cavity (δ_{cavity}) and the car body ($\delta_{car\ body}$) were conducted. As depicted in Figure 13(b), the δ_{bogie} remains positive and experiences a rapid increase in the jet velocity at various jet angles. Conversely, the δ_{cavity} decreases rapidly from a positive value at a jet velocity of $0.2U$ to negative with values increase with increasing velocities, as illustrated in Figure 13(c). In comparison to the changes in δ_{bogie} and δ_{cavity}, the variation observed for the car body is relatively minor, with a maximum $\delta_{car\ body}$ variation of less than 1%, as shown Figure 13(d). Due to the greater increasing reduction rate in aerodynamic drag for the bogie compared to the decrease for the cavity, the overall aerodynamic resistance exhibits a reduction effect as the jet velocity increases.

Figure 14 shows the power spectral density (PSD) of the aerodynamic drag for the leading bogie and the head coach of the train, where the x-coordinate is the Strouhal number (St). In the absence of the air-jet, the main St for the leading bogie ranges from 0.05 to 0.16, while the maximum PSD peak for the head coach occurs at St of 0.14. When applying air-jet with increasing velocities in front of the leading bogie, the main variation frequency

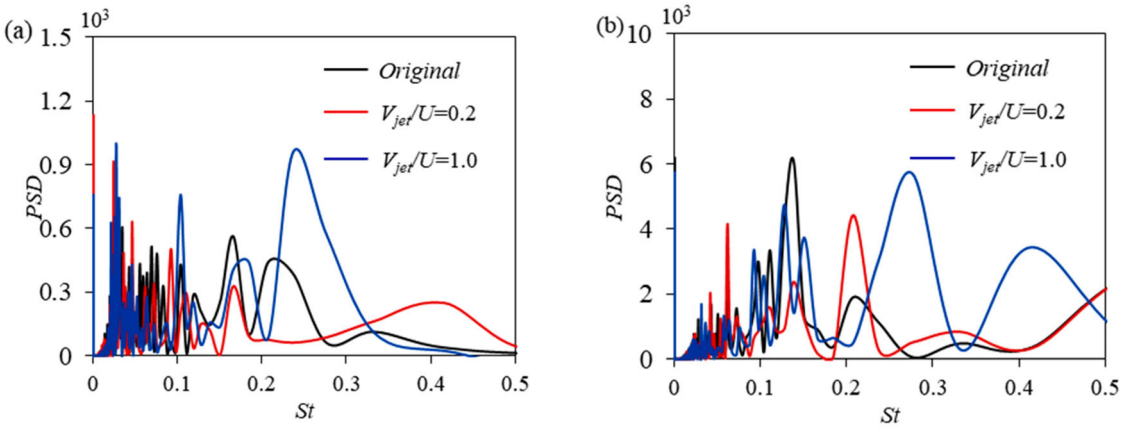

Figure 14. Power spectral density of the aerodynamic drag: (a) the leading bogie; (b) the head coach.

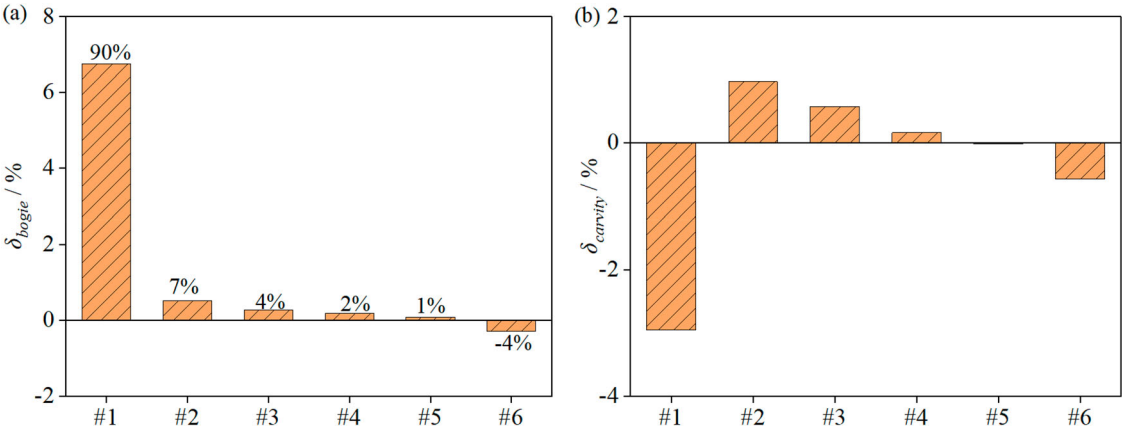

Figure 15. Reduction rates in aerodynamic drag for individual bogies and cavities at $V_{jet}/U = 0.8$ and $\alpha = 15°$:(a) the bogies; (b) the cavities.

gets larger, *St* reaches approximately 0.24 and 0.27 for the leading bogie and the head coach as the jet velocity increases to 1.0*U*.

Figure 15 compares the reduction ratio of aerodynamic drag for individual bogies and cavities at various positions, considering a jet velocity and angle of $V_{jet}/U = 0.8$ and $\alpha = 15°$. The findings indicate that the impact of the jet flow on individual bogies gradually diminishes as the bogie position moves towards the rear of the train. Specifically, the leading bogie accounts for 90% of the overall reduction in aerodynamic drag among the bogies. Similarly, the first cavity significantly contributes to the overall variation in aerodynamic drag among the cavities. To summarize, the aerodynamic performance of the bogie and surrounding cavities are significantly influenced by the implementation of jet flow in front of the leading bogie, while its impact on the train body is minimal. Consequently, the subsequent analysis of the flow field primarily concentrates on the leading bogie and cavity region.

The flow velocity and surface pressure distribution in the leading bogie region with and without the air-jet are demonstrated in Figure 16. In the absence of jet flow control, the main streamwise flow accelerates towards the bottom of the train and exerts a direct impact on the lower portion of the bogie (the region located outside the cavity, denoted as *A1*∼*A3* in Figure 16) as well as the rear end of the cavity (denoted as *A4* in Figure 16), resulting in significant positive pressures. Meanwhile, the streamwise flow separates at the bottom edge of the frontal end of the cavity, leading to a decrease in velocity within the cavity, the pressure distributed on the upper section of the bogie and the frontal end of the cavity are predominantly negative. Additionally, the flow underneath the vehicle traverses a multitude of complex components and diverges at the trailing edge, resulting in negative pressures on the leeward side of the bogie. The disparities in the pressure between the windward and leeward surfaces of the bogie, as well as between both ends of the cavity contribute to significant aerodynamic drag. Viscous drag resulting from wall shear stress also contributes to the total aerodynamic resistance. As indicated in Figure 17(a), regions including the streamlined head, the leading bogie and the lower surface posterior

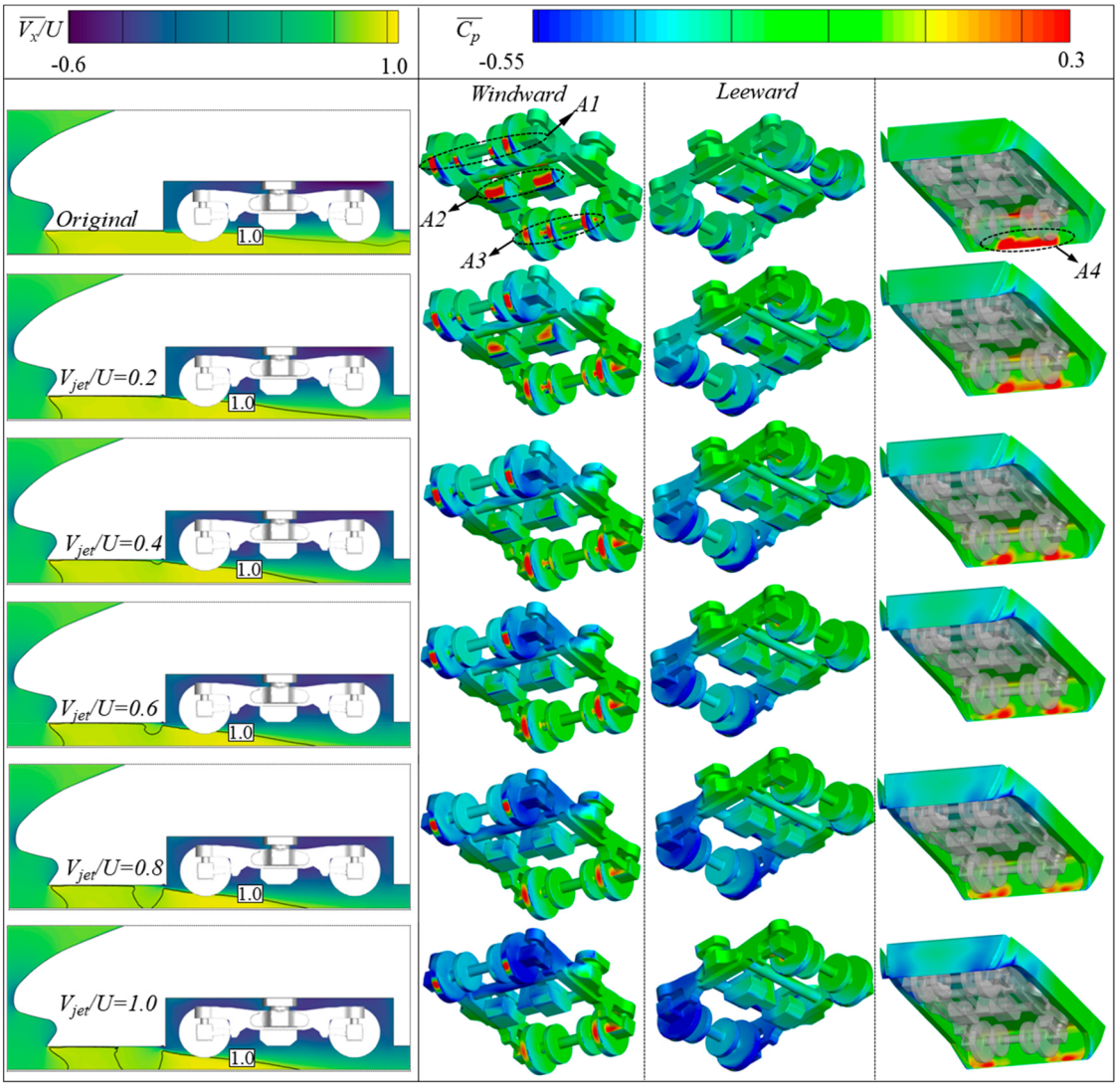

Figure 16. Mean flow velocity and surface pressure distributions in bogie and cavity regions under different jet flow velocities at an angle of $\alpha = 15°$.

to the cavity of the head coach exhibit relatively high shear stress, while other areas display lower values. However, according to the computational results, pressure drag remains the dominant component, accounting for approximately 70% of the total aerodynamic resistance.

Introducing an air-jet in front of the leading bogie slightly changes the mean wall shear stress distribution along the bottom of the train head. As shown in Figure 17(b–f), increasing jet velocities reduce mean wall shear stress in region *A4* (the central component of the bogie) and region *A5* (spanwise centre of the head coach's lower surface), thereby decreasing the viscous drag of the train. However, changes in pressure are more complex, pressure changes on both the bogie and cavity ends are not consistent with jet velocities. In order to conduct a quantitative analysis, the time averaging *x*-component of flow velocity along two spatial vertical lines (referring to *X1* and *X2* in Figure 18) in the cavity region before and after the bogie, and the pressure distribution along two surface vertical lines located on both ends of the cavity (referring to *X3* and *X4* in Figure 18) are demonstrated in Figure 19 and 20.

Based on the extensive analysis conducted from Figure 16–20, it can be inferred that the introduction of a jet flow in front of the leading bogie obstructs the streamwise underbody flow to some extent. Combined with the analysis of synthesis velocity in Figure 21, the angle of the synthetic flow β increases as the jet velocity rises, resulting in a continuous downward movement of the streamwise flow at the bottom. Consequently, the airflow velocity in the lower section of the bogie, particularly in the region between the bottom of the wheel (*BOW*) and the bottom of the cavity, experiences a gradual reduction, with the magnitude of reduction intensifying with

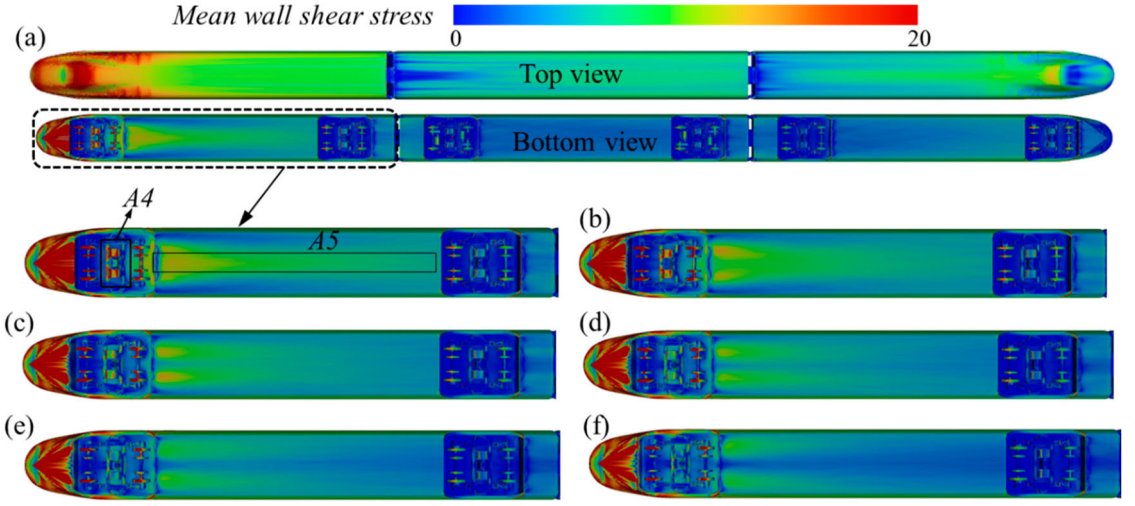

Figure 17. Mean wall shear stress contours distributed at the bottom of the head under various jet velocities at an angle of $\alpha = 15°$: (a) original case without air-jet; (b) $V_{jet}/U = 0.2$; (c) $V_{jet}/U = 0.4$; (d) $V_{jet}/U = 0.6$; (e) $V_{jet}/U = 0.8$; (f) $V_{jet}/U = 1.0$.

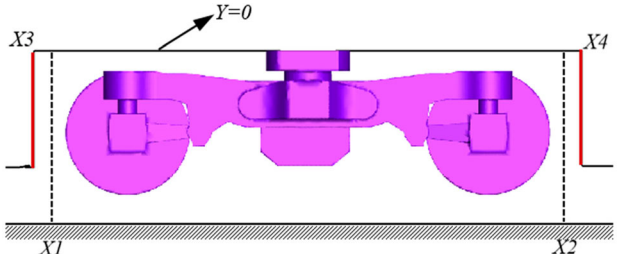

Figure 18. Positions of spacial lines and surface lines.

the jet velocity due to the heightened obstruction effect caused by the higher jet velocity, while the variation in flow velocity along *X1* in the cavity region is relatively small. As the flow moves towards the rear of the bogie, the reduction in flow velocity becomes more significant, and the velocity distribution along *X2* exhibits a rapid decline as the jet velocity increases, eventually reaching negative values (flow in the reverse direction) within the cavity when the jet velocity surpasses 0.2*U*. The noticeable decrease in velocity at the lower section of the bogie leads to a substantial decrease in the positive pressure exerted on the windward surface of the bottom components, particularly in region *A2*, where the front air velocities decrease rapidly from positive to negative as the jet velocity increases. Additionally, when the flow velocity at the wake of the bogie decreases from positive to negative, the pressure on the leeward surface of the bogie undergoes an increase from negative to positive value due to the influence of reverse flow. This reverse flow also leads to a decrease in pressure on the windward side as it passes over the blunt components of the bogie toward the front. As the windward surface of the bogie experiences a continuous decrease in pressure and the leeward side experiences an increase, the aerodynamic drag of the bogie exhibits a progressively increasing drag reduction rate with the increasing jet velocity.

The variation in flow velocity also induces a discernible change in pressure on both ends of the cavity. As depicted in Figure 22, the underbody streamwise flow moves downwards gradually under the intensifying jet flow, the frontal low-speed air within the cavity is entrained by the downward streamwise flow, resulting in an increase in the flow velocity along *X1* within the cavity region, thereby amplifying the negative pressure distributed along *X3* on the front end of the cavity as the jet velocity increases. Moreover, in the absence of jet flow, the underbody flow exerts a direct impact on the bottom rear end of the cavity, the air is subsequently rolled up to form an counter-clockwise rotating vortex, thus the distribution of pressure along *X4* on the rear end of the cavity gradually decreases from a large positive value to a negative value as the height increases, then it increases once again to a positive value in the top corner of the cavity where the air is stagnated. However, under the impact of jet flow with increasing speed, the rolled-up air is hindered by the intensified downward streamwise flow, potentially causing it to be diverted in the opposite direction, and this diversion results in a significant reduction in the flow velocity along *X2*. Subsequently, the decrease of flow velocity along *X2* leads to a decrease in pressure along *X4* on the rear end of the cavity, especially at the bottom region *C4*. Since the decrease in positive pressure on the rear end of the cavity is accompanied by an increase in negative pressure on the front end, making it challenging to ascertain the changes in drag of the cavity with jet velocity. Consequently, the pressure disparity between the front and rear ends of the cavity is calculated and illustrated in Figure 23, comparisons reveal that the reduction in positive pressure on the rear end of the cavity

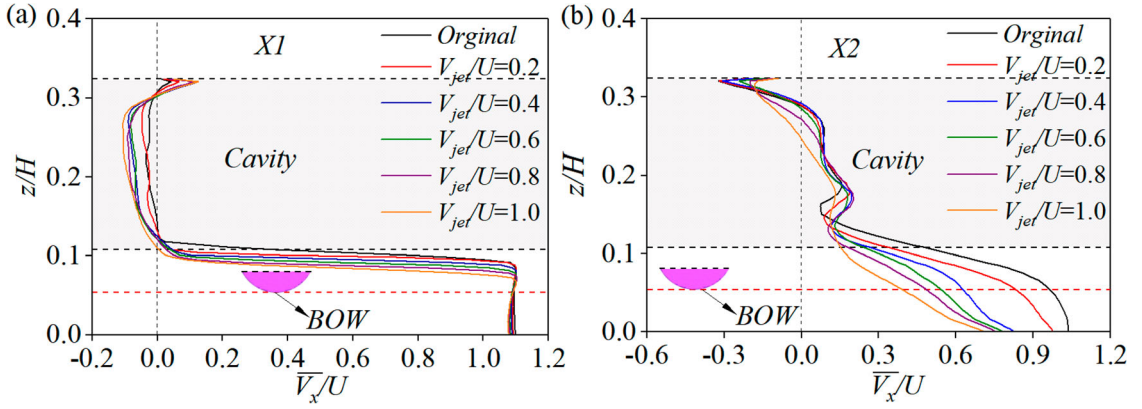

Figure 19. Time-averaged velocity distributions along vertical lines in the cavity region at various jet velocities at $\alpha = 15°$: (a) along *X1*; (b) along *X2*.

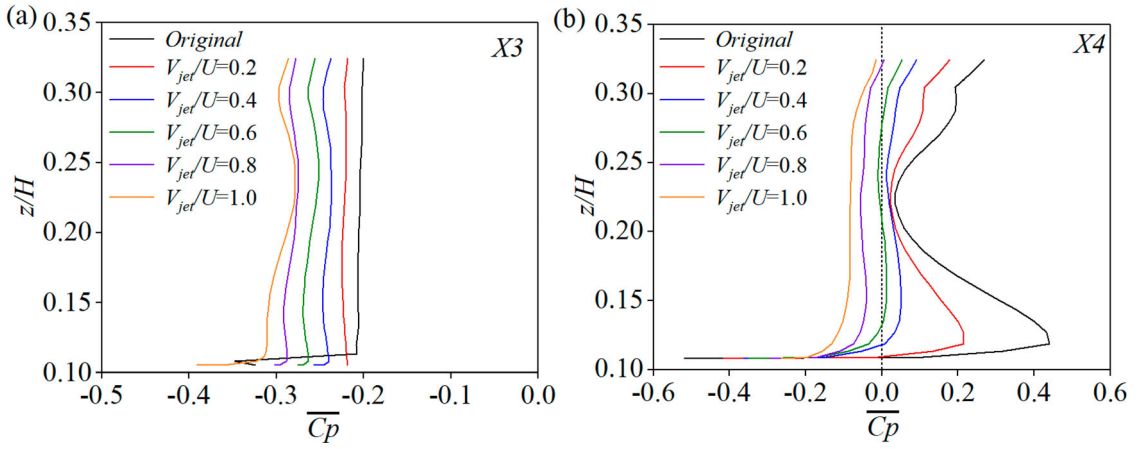

Figure 20. Time-averaged pressure distributions along surface lines on both ends of the cavity at various jet velocities at $\alpha = 15°$: (a) along *X3*; (b) along *X4*.

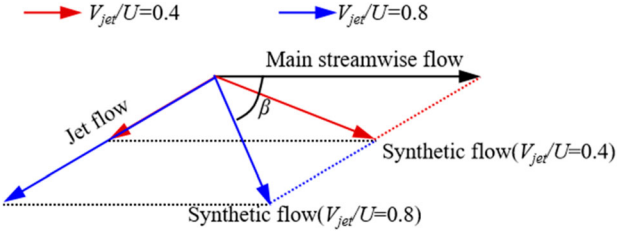

Figure 21. Synthetic velocity under different jet velocities.

is comparatively smaller than the increase in negative pressure on the front end. This pressure difference progressively intensifies as the jet velocity increases, leading to an escalation in the drag of the cavity.

3.1.2. Effect of jet angle

Referring to the aerodynamic drag reduction results at varying jet velocities and angles in Figure 13, the observed change pattern of δ with jet angle is characterized by fluctuations rather than a monotonic trend, and the disparity in drag reduction rates caused by varying jet angles remains within a range of 2.4% at a specific jet velocity. When the jet velocity is less than $0.8U$, the δ_{total}at jet angle of 90° is the smallest, while it's maximum value remains at jet angle of 15°. However, when the jet velocity exceeds $1.0U$, jetting at angle of 90° exhibits better drag reduction effect with continuous increasing reduction rate in aerodynamic drag. The δ_{bogie} basically exhibits a slight decrease as the jet angle increases. However, the influence of jet angle on the δ_{cavity} does not display a constant pattern of increase or decrease, but fluctuates with amplitudes below 2%.

Although the influence of jet angle is not as significant as the jet velocity, this study also examined the surface pressure and flow velocity at jet angles of $\alpha = 15°$ and $\alpha = 90°$. As indicated in Figure 24 and 25, the angle and velocity of the synthetic flow increase as the jet angle increases, leading to an downward movement of the underbody streamwise flow. Since the x-component of the jet velocity which flows in the opposite direction to the incoming flow decreases, resulting in a weakened hindrance to the streamwsie flow at front of the jet slot.

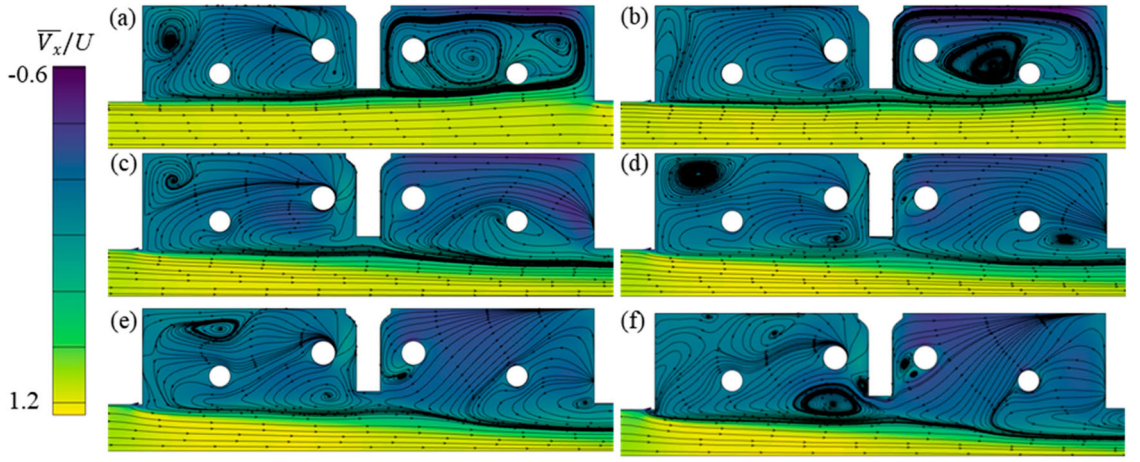

Figure 22. Time-averaged velocities and streamlines in the leading bogie region under different jet velocities: (a) original train without jet; (b) $V_{jet}/U = 0.2$; (c) $V_{jet}/U = 0.4$; (d) $V_{jet}/U = 0.6$; (e) $V_{jet}/U = 0.8$; (f) $V_{jet}/U = 1.0$.

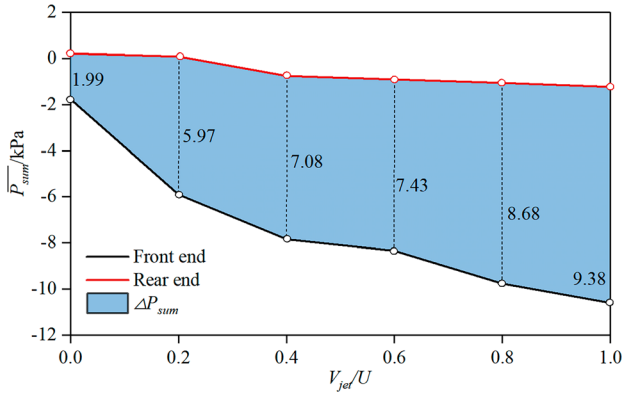

Figure 23. Pressure disparities between the front and rear ends of the cavity at varying jet velocities.

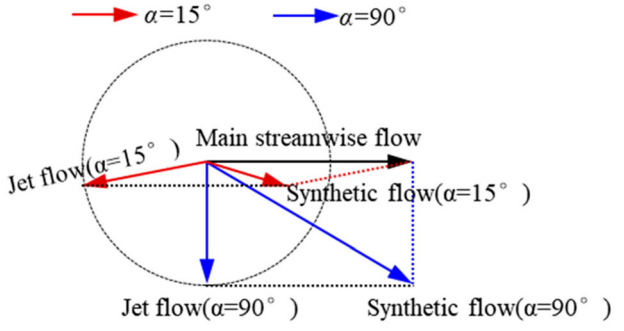

Figure 24. Synthetic velocity under different jet angles.

Subsequently, there is a slight increase in the flow velocity along *X1* in the lower section of the bogie followed by an increase near the bottom floor of the train due to the rising synthetic velocity near the jet slot. Furthermore, the increasing synthetic velocity draws in more air from the cavity, leading to a decline in flow velocity in the frontal cavity region. This decrease in flow velocity results in a reduction in the negative pressure distributed on the

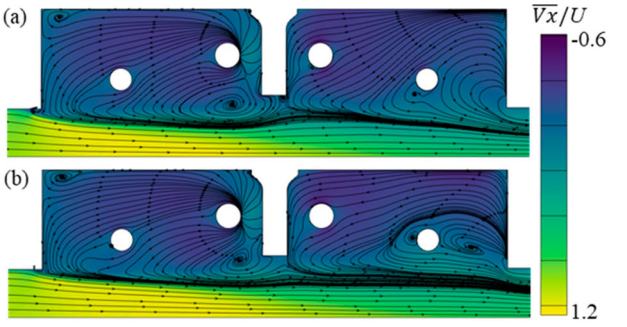

Figure 25. Streamlines in the cavity and bogie region under different jet angles: (a) $\alpha = 15°$; (b) $\alpha = 90°$.

front end of the cavity and an increase on the windward surface of the bogie, as shown in Figure 26(a). The flow velocity along *X2* in Figure 26(b) exhibits a comparable change pattern to that of *X1*, resulting in increased positive pressure at the lower section and decreased negative pressure at the upper section of the rear end of the cavity. Additionally, the decrease in negative velocity in the rear cavity region contributes to a reduction in the distribution of negative pressure on the leeward side of the bogie, as depicted in Figure 27 and 28. By calculating the sum of pressure on the front and rear ends of the cavity in Figure 29, it is evident that an approximate equilibrium pressure difference is achieved, thereby causing minimal alternation in the δ_{cavity} as the jet angle increases from 15° to 90°, while the δ_{bogie} increase with smaller disparity of 1.9%.

3.2. Impact of air jet on the slipstream of the train

3.2.1. Effect of jet velocity

The underbody vortexes characterized by Q ($Q = 1 \times 10^5$), and the vorticity magnitude beneath the head coach

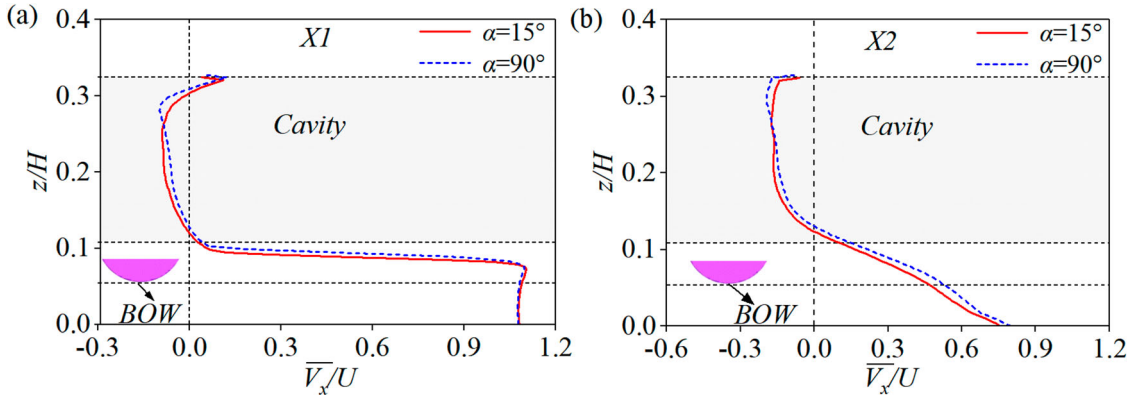

Figure 26. Velocity distributions along vertical lines in cavity region at various jet angles at $V_{jet}/U = 0.8$: (a) along *X1*; (b) along *X2*.

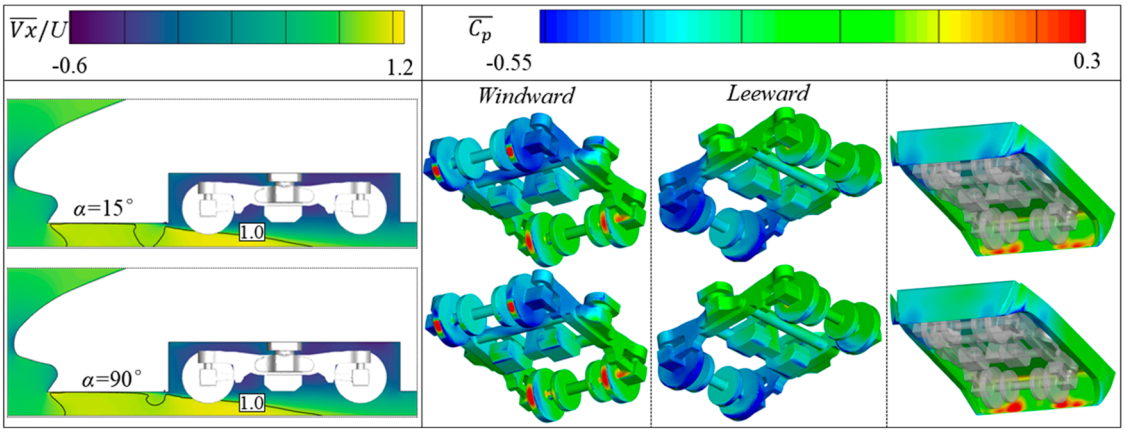

Figure 27. Time-averaged flow velocity and surface pressure distributions in bogie and cavity regions under different jet angles at velocity of $V_{jet}/U = 0.8$.

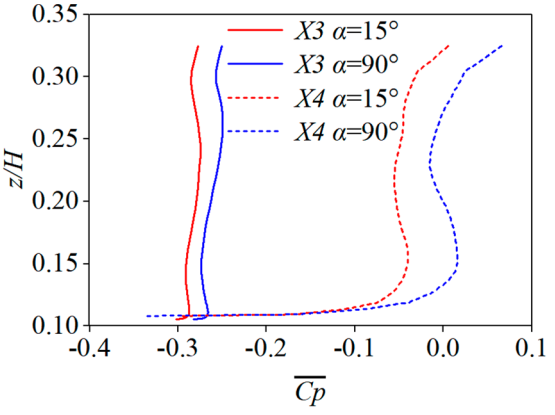

Figure 28. Pressure distributions along surface lines on the front and rear ends of the cavity at various jet angles at $V_{jet}/U = 0.8$.

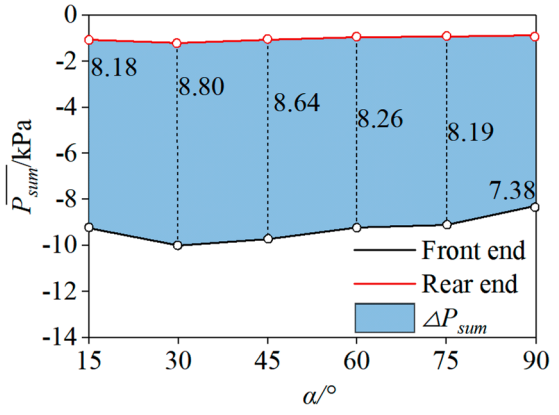

Figure 29. Pressure disparities between the front and rear ends of the cavity at varying jet angles.

($Z = 0.07H$) at varying jet velocities are demonstrated in Figure 30. For the original train without air jet, a pair of triangular vortex structures (*V1*) developing sideward are generated in region *R1*, exhibiting high vorticity magnitude. A series of small vortexes are formed and accumulated in the bogie region as the underbody flow traverses the front end of the cavity. When introducing an air jet in front of the leading bogie, the triangular vortexes in *R1* are depressed to some extend, and the vorticity decreases slightly. As the jet velocity increases, the small-scale vortices in the bogie region merge with those generated by jet flow that evolves forward by the streamwise flow, the vorticity intensities are intensified after the jet slot in *R2*. The turbulent intensity (TI) and turbulent

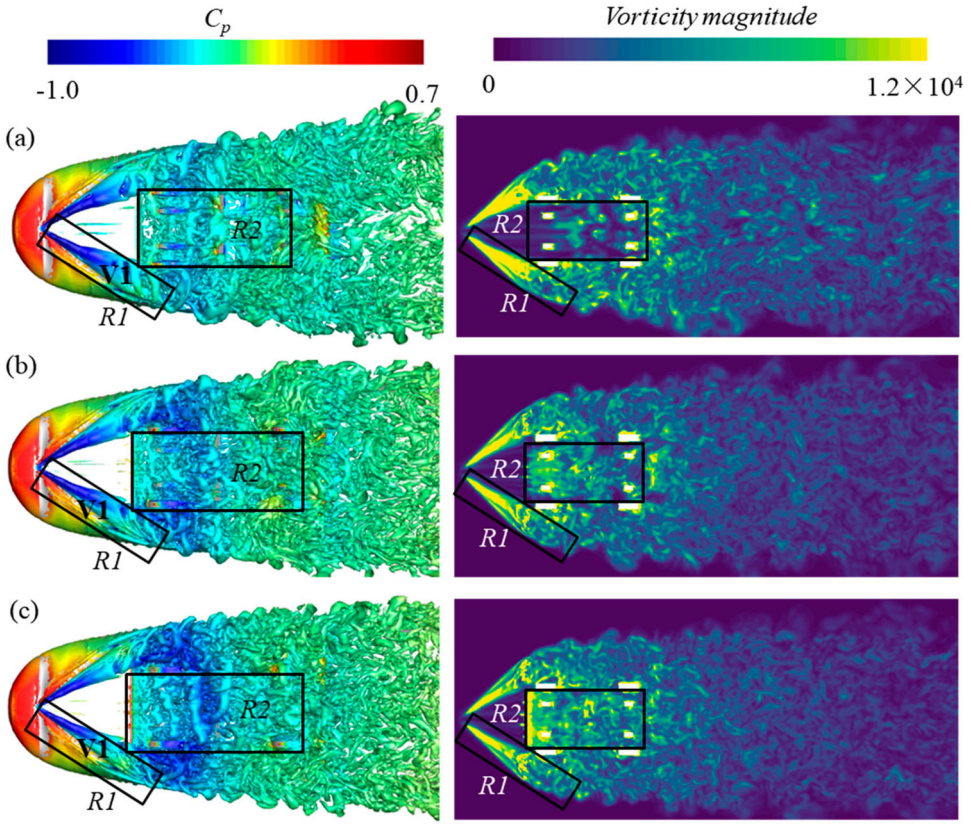

Figure 30. Iso-surface of Q ($Q = 1 \times 10^5$) and vorticity magnitude under air jet of $\alpha = 15°$: (a) original train without air-jet; (b) $V_{jet}/U = 0.4$; (c) $V_{jet}/U = 0.8$.

kinetic energy (TKE) are also demonstrated in Figure 31. The TI and TKE in region *R1* (where the main triangular vortexes located) slightly decreases, and the wake length of the sideward strong turbulent intensity region decreases, seen from *l1* to *l3*. Meanwhile, the TI and TKE in region *R2* after the jet slot (where bogies located) rises, which indicates that the presence of an air jet results in heightened turbulent strength in the bogie region after the jet slot compared to conditions without air jet. However, the increases in vorticity magnitude, TI and TKE are limited to the bottom bogie region after the jet slot, these turbulent variables in majority regions barely changes and remains consistent.

However, the above analysis can't tell the amplitude changes of slipstreams under impact of varying jet velocities, thus the time-averaged horizontal slipstream velocities $\overline{V_{xy}}$ along the longitudinal direction at four positions under air-jet angle of 15° are displayed in Figure 33. The position of the four longitudinal lines, marked *C1-C4,* are presented in Figure 32, among which *C1* and *C2* are located at heights of $0.03H$ and $0.07H$ from the top of the ground (TOG) in the spanwise center underneath the train, while *C3* and *C4* are located on the trackside with lateral distance of $0.5H$ from the COT and heights of $0.07H$ and $0.15H$ from the TOR.

As indicated in Figure 33(a) and (b), in the absence of jet flow control, the velocity of incoming flow initially decreases in front of the head nose, then moves rapidly at an accelerating speed to the bottom of the train. Once the streamwise air flows to the bogie region, the underbody slipstream velocity experiences a gradual decrease due to the sudden expansion of space. Subsequently, it remains fluctuation in the 2nd and 3rd bogie regions and experiences another slight increase under the middle coach. After another fluctuation in the 4th and 5th bogie region, the slipstream velocity continuously increases until the underbody air reaches the last bogie region, then it decreases rapidly to the minimum peak and rises again in the wake region. when implementing an air-jet in front of the leading bogie, large disparity in the slipstream velocities occurs underneath the head coach, especially in the region after the position of the jet (POJ), $\overline{V_{xy}}$ significantly decreases as the jet velocity increases under the obstruction effect of the jet flow, the impact of the jet flow on the underbody slipstream velocity toward the rear of the train gradually weakens. The variations of the trackside slipstream velocities are relatively small, except for slight increase in the leading bogie region after the jet slot, as indicated in Figure 33(c) and (d). Figure 34 gives the time-averaged streamwise and

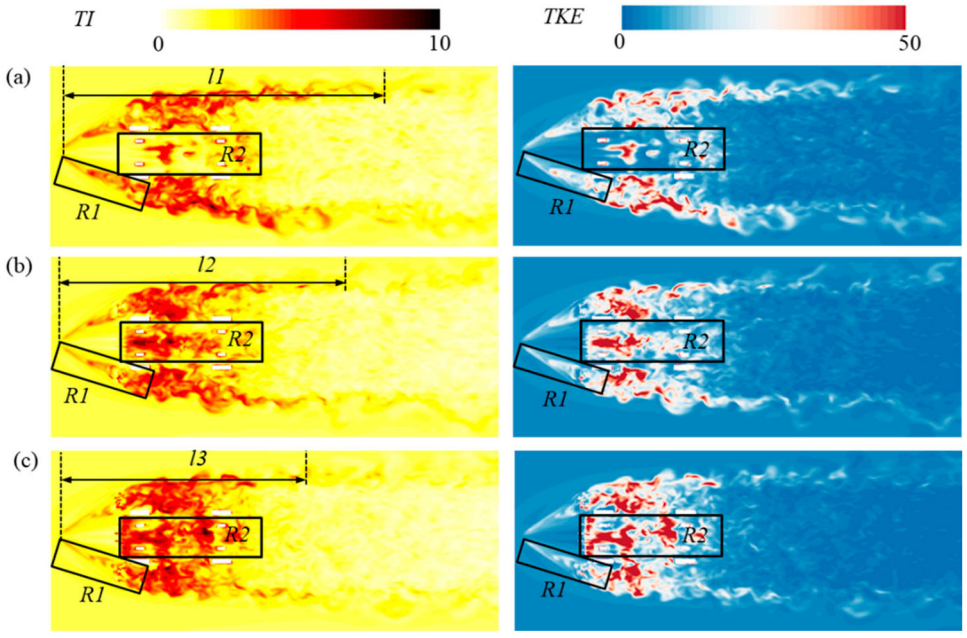

Figure 31. Turbulent intensity (TI) and turbulent kinetic energy (TKE) under air jet of $\alpha = 15°$: (a) original train without air-jet; (b) $V_{jet}/U = 0.4$; (c) $V_{jet}/U = 0.8$.

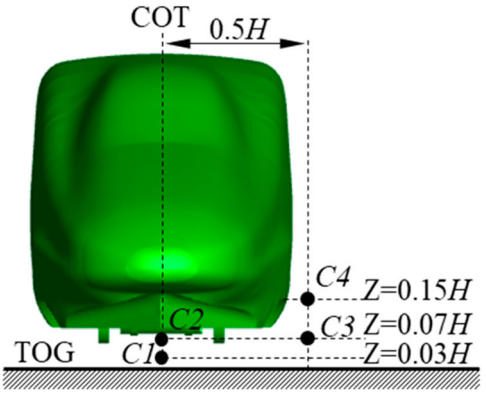

Figure 32. Positions of the slipstream lines.

spanwise velocity ($\overline{V_x}$ and $\overline{V_y}$, respectively) contours on a horizontal plane $Z = 0.07H$ (height of line *C2* and *C3*) under different jet velocities. Under the interference of the triangular guide structure at the bottom of the train, the underbody airflow accelerates towards both forward and sideward at a certain angle corresponding to the guide structure, and two symmetrical long-strip deceleration zones are generated at the transition areas between the bottom guide structure and the train body. The central $\overline{V_x}$ along the longitudinal line *C2* decreases with the distance away from the head nose. When setting an air-jet in front of the bogie at angle of 15°, the x-component of the jet velocity was opposite to the incoming flow and the z-component of the jet velocity obstructs the streamwise movement of the incoming flow, resulting in an decrease in the slipstream velocity before and after the jet slot, especially in the afterwards region, and the decrease effect enhances with the increase of the jet velocity. However, the velocity in the deceleration zones increases with the jet velocity, which leads to a slight increase in the trackside slipstream velocity of line *C3* in the bogie region. The effect of air jet on the $\overline{V_y}$ is minimal, the only difference occurs near the jet-slot region with slight increase.

3.2.2. Effect of jet angle

Figure 35 and 36 also give the underbody vortexes, vorticity magnitudes, turbulent intensities and turbulent kinetic energy under varying jet angles at $V_{jet}/U = 0.8$. It is obvious that the effect of jet angle on the transient fluctuation characteristics of the underbody flow is minimal compared to the jet velocity. As the jet angle increases, the vortex vorticity, TI and TKE slightly underneath the head coach remain the same, except for a slight decrease in a small region *R3* after the jet slot. Since increasing the jet angle at a constant flow rate minimally enhances the jet energy to disturb the bottom flow, but only slightly obstructs the air flowing to the front edge of the cavity, thus suppressing the intensity of vortexes at the front ends.

Figure 37 demonstrates the mean slipstream velocities at various jet angles with a velocity of $V_{jet}/U = 0.8$. It is evident that the impact of the jet angle on the slipstream velocity beneath the train is less pronounced compared to the jet velocity. Variations in $\overline{V_{xy}}$ are primarily observed in the region after the leading bogie, with a

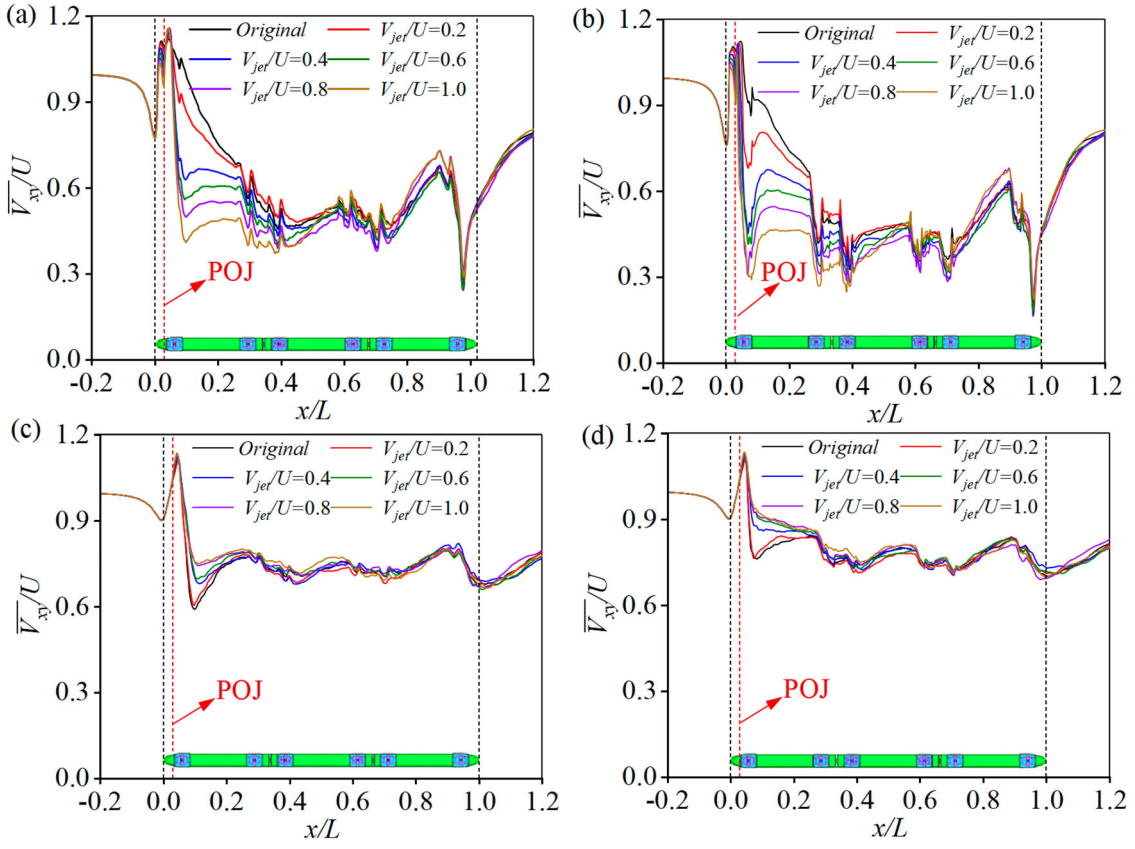

Figure 33. Time-averaged slipstream velocities along the longitudinal direction under varying jet velocities: (a) *C1*; (b) *C2*; (c) *C3*; (d) *C4*.

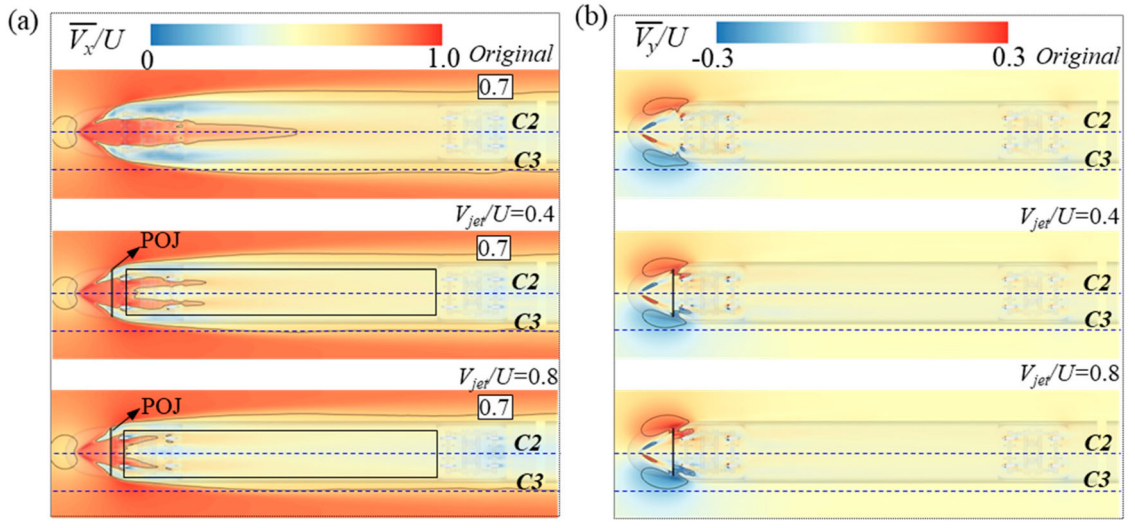

Figure 34. Time-averaged streamwise and spanwise velocity contours on a horizontal plane Z = 0.07H: (a) $\overline{V_x}$; (b) $\overline{V_y}$.

gradual increase with the increasing jet angle and gets more significant when it reaches 90°. Due to the narrow width of the jet slot relative to the underbody space, the energy of the vertical jet-flow ($\alpha = 90°$) is insufficient to completely impede the streamwise flow, resulting in a less significant obstructive effect compared to the revers flow ($\alpha < 90°$), the underbody slipstream velocity is lower under small jet angles. The trackside slipstream velocities show a consistent change law and approximate equal peak values under varying jet angels.

4. Conclusions

To explore the potential and effectiveness of jet flow control technology in optimizing the flow field in bogie regions and subsequently reducing the aerodynamic

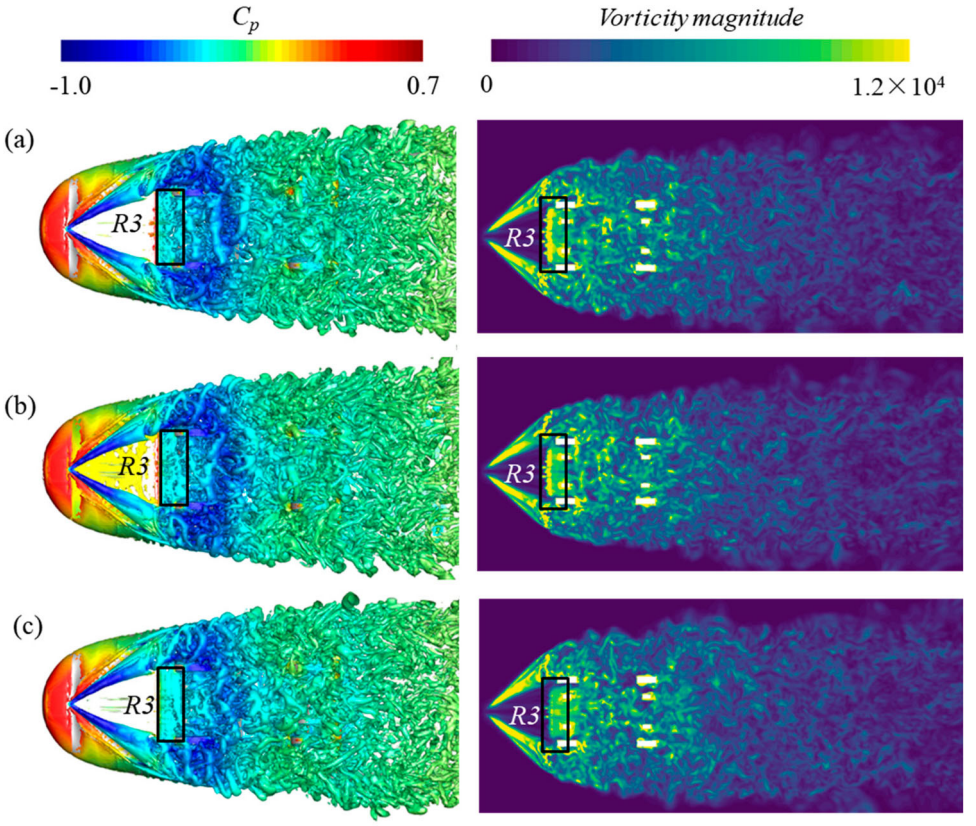

Figure 35. Iso-surface of Q ($Q = 1 \times 10^5$) and vorticity magnitude under air jet of $V_{jet}/U = 0.8$: (a) $\alpha = 15°$; (b) $\alpha = 45°$; (c) $\alpha = 90°$.

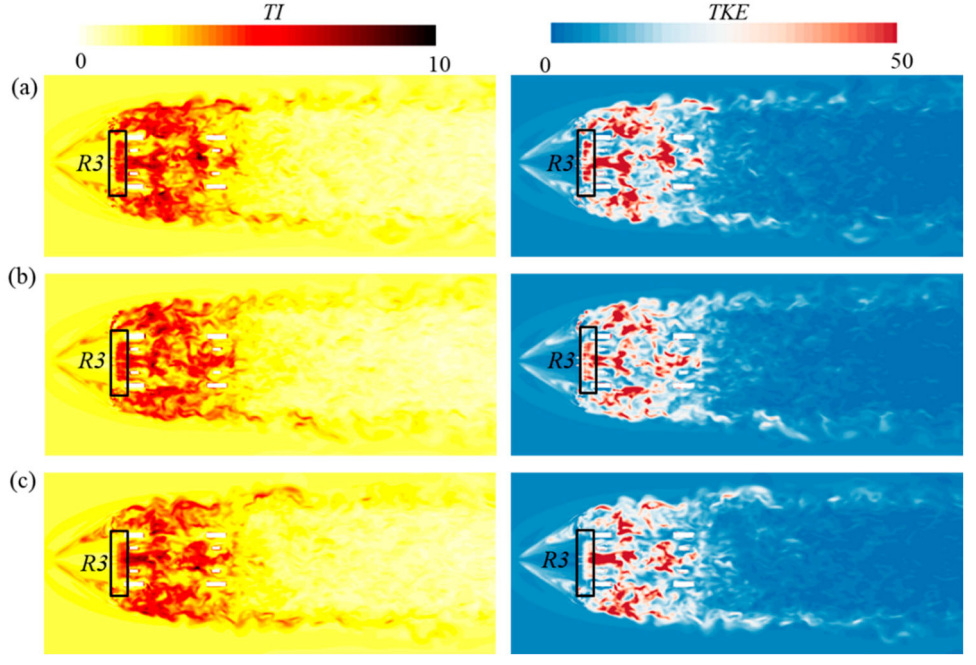

Figure 36. Turbulent intensity (TI) and turbulent kinetic energy (TKE) under air jet of $V_{jet}/U = 0.8$: (a) $\alpha = 15°$; (b) $\alpha = 45°$; (c) $\alpha = 90°$.

resistance of high-speed train, an air jet slot was applied in front of the leading bogie in this study, effects of jet velocities and angles on the underbody slipstream of the train were investigated, and potential of aerodynamic drag reduction were discussed. Conclusions are drawn as follows:

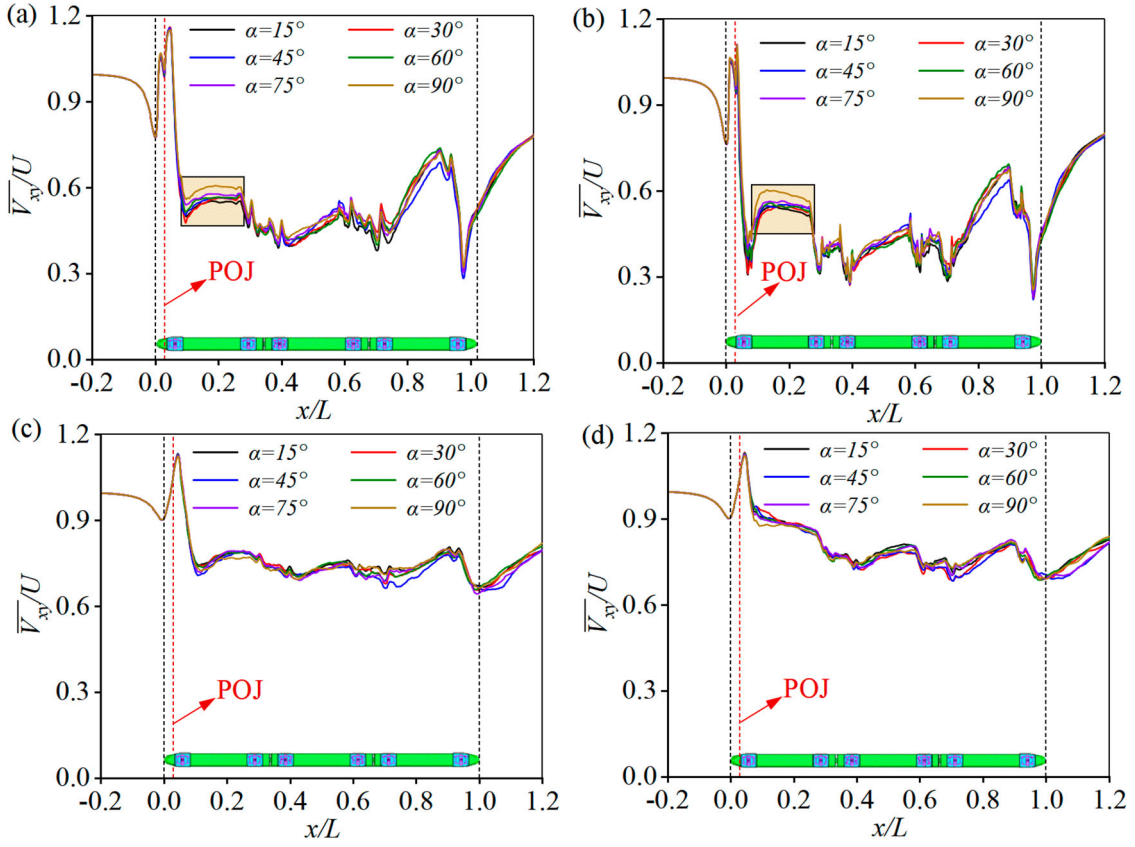

Figure 37. Time-averaging slipstream velocities along the longitudinal direction under varying jet angles: (a) *C1*; (b) *C2*; (c) *C3*; (d) *C4*.

(1) Setting an air jet in front of the leading bogie is effective in reducing the aerodynamic drag of the train. The overall drag reduction rate (δ) demonstrates a notable upward trajectory with increasing jet velocity, followed by a slight decrease until it reaches $0.8U$ at jet angle below 75°. However, the behaviour differs at jet angle of 90°, as it consistently exhibits an increasing trend with jet velocity. The overall drag reduction mainly owes to greater decrease in the aerodynamic drag of the bogies than the increase in cavities.

(2) The impact of jet angle is less pronounced compared to jet velocity. The δ changing with jet angle is characterized by fluctuations rather than a monotonic trend, but the disparities caused by varying jet angles remain within a range of 2.4% at a specific jet velocity. The maximum δ appears at jet angle of 15° when the jet velocity is less than $0.8U$, but jetting at an angle of 90° exhibits a better drag reduction effect with continuously increasing reduction rate in aerodynamic drag as the jet velocity exceeds $0.8U$.

(3) The increasing jet velocity leads to a significant decrease in the slipstream velocity under the head coach after the jet slot due to its evident obstruction effect, while variations of the trackside slipstream velocities are relatively small, except for a slight increase in the leading bogie region after the jet slot. The influence of jet angle on the transient and time-averaged underbody slipstream is minimal compared to the jet velocity.

(4) Increasing jet velocities increase the vortex vorticity, turbulent intensity and turbulent kinetic energy under the leading bogie region. However, the increase of jet angles slightly decreases those in a small region right after the jet slot.

(5) The most effective aerodynamic drag reduction is achieved at a jet velocity of $0.8U$ and jet angle of 15°, with a maximum reduction rate of 6.43%. However, a notable increase in the turbulent intensity under the leading bogie was observed at higher jet velocities, which should be paid attention to avoid transient instability.

This paper proposes a novel approach to reduce the train's aerodynamic resistance by implementing an air jet in front of the leading bogie, and the effects of jet velocities and angles on the underbody slipstream and aerodynamic drag are thoroughly examined. However, this paper focused solely on the impact of jet flow control at a single position in front of the leading bogie,

other positions or multiple positions were not investigated due to the paper's length limitation, which is worthy to be further explored in future research. Besides, this paper only investigates jet velocities smaller than the train speed, higher velocities are not considered due to its extra greater energy input, which may consequently reduce the efficiency of energy savings. More studies considering more jet velocities, slot widths, and unsteady flowing modes should carried out in the future. Furthermore, due to the heightened turbulent intensity beneath the bogie at increased jet velocities, it is advisable to implement additional deflectors in combination with the jet flow technique to enhance the drag reduction and stability performance. These deflectors may located at the front ends of the cavity to suppress leading edge separation, or pursue the bottom plate to regulate the complex flow structures underneath the bogie. Future research should focus on the mutual coupling mechanism between active and passive flow control to provide guidance for the scheme designs.

Acknowledgments

The authors thank the Big Data Center for Boimedical Research of Wuyi University for providing computing resources.

Disclosure statement

No potential conflict of interest was reported by the author(s).

CRediT authorship contribution statement

Sha Huang: Conceptualization, Methodology, Formal analysis, Writing-Original draft. **Zhi-Wei Li:** Methodology, Supervision, Writing – review & editing. **Wen-Jing Peng:** Investigation, Validation. **Jin-Rong Lin:** Data curation, Visualization. **Zun-Di Huang:** Writing – review & editing. **Guang-Zhi Zeng:** Investigation, Visualization.

Funding

This work was supported by the National Science Foundation of Guangdong Province under [grant number 2022A1515010011]; the Jiangmen Basic and Theoretical Science Research Project (2023) under [grant number 2023JC01020]; and the Hong Kong and Macao Joint Research and Development Fund of Wuyi University under [grant number2019WGALH17].

Data availability statement

The data that support the findings of this study are available from the corresponding author, Z. W. Li, upon reasonable request.

References

Ansys, Inc. (2019). Ansys Fluent. https://www.ansys.com/products/fluids/ansys-fluent.

Aultman, M., Wang, Z. Y., Auza-Gutierrez, R., & Duan, L. (2022). Evaluation of CFD methodologies for prediction of flows around simplified and complex automotive models. *Computers & Fluids*, *236*, 105297. https://doi.org/10.1016/j.compfluid.2021.105297

Bao, S. J., Hu, X., Wang, J. K., Ma, T. H., Rao, Y. Y., & Deng, Z. G. (2020). Numerical study on the influence of initial ambient temperature on the aerodynamic heating in the tube train system. *Advances in Aerodynamics*, *2*(1), 28. https://doi.org/10.1186/s42774-020-00053-8

Celik, I. B., Ghia, U., Roache, P. J., & Freitas, C. J. (2008). Procedure for estimation and reporting of uncertainty due to discretization in CFD applications. *Journal of Fluids Engineering*, *130*(7), 078001. https://doi.org/10.1115/1.2960953

CEN European Standard. (2013). Railway application - aerodynamics. Part4: Requirements and test procedures for aerodynamics on open track. BS EN 14067-4: 2013.

Che, Z. X., Chen, Z. W., Ni, Y. Q., Huang, S., & Li, Z. W. (2023a). Research on the impact of air-blowing on aerodynamic drag reduction and wake characteristics of a high-speed maglev train. *Physics of Fluids*, *35*(11), 115138. https://doi.org/10.1063/5.0175323

Che, Z. X., Huang, S., Li, Z. W., & Chen, Z. W. (2023b). Aerodynamic drag reduction of high-speed maglev train based on air blowing/suction. *Journal of Wind Engineering and Industrial Aerodynamics*, *233*, 105321. https://doi.org/10.1016/j.jweia.2023.105321

Chen, Z. W., Guo, Z. J., Che, Z. X., Huang, Z. D., Ni, Y. Q., Wang, S. M., Huang, S., Li, Z. W., & Wang, Q. X. (2024). Evaluation of active leeward side air-blowing layout on the lateral aerodynamic performance of high-speed trains in crosswinds environment: Sustainable and safe operation strategy. *Journal of Wind Engineering and Industrial Aerodynamics*, *247*, 105695. https://doi.org/10.1016/j.jweia.2024.105695

Chen, Z. W., Ni, Y. Q., Wang, Y. W., Wang, S. M., & Liu, T. H. (2022). Mitigating crosswind effect on high-speed trains by active blowing method: a comparative study. *Engineering Applications of Computational Fluid Mechanics*, *16*(1), 1064–1081. https://doi.org/10.1080/19942060.2022.2064921

Chen, Z. W., Zeng, G. Z., Ni, Y. Q., Liu, T. H., Niu, J. Q., & Yao, H. D. (2023). Reducing the aerodynamic drag of high-speed trains by air blowing from the nose part: Effect of blowing speed. *Journal of Wind Engineering and Industrial Aerodynamics*, *238*, 105429. https://doi.org/10.1016/j.jweia.2023.105429

China National Railway Administration. (2018). Railway application – Aerodynamics – Part 4: Requirements fro train aerodynamic simulation, TB/T 3503.4-2018.

Choi, J. N., & Lee, J. H. (2023). Active control of pressure fluctuations in an incompressible turbulent cavity flow. *Aerospace Science and Technology*, *141*, 108512. https://doi.org/10.1016/j.ast.2023.108512

Cui, H. J., Chen, G. X., Guan, Y., & Deng, W. (2023). Study on aerodynamic drag reduction at tail of 400 km/h EMU with air suction-blowing combination. *Machines*, *11*(2), 222. https://doi.org/10.3390/machines11020222

Dai, Z. Y., Li, T., Zhang, W. H., & Zhang, J. Y. (2024). Investigation on aerodynamic characteristics of high-speed trains with shields beneath bogies. *Journal of Wind Engineering and Industrial Aerodynamics*, *246*, 105666. https://doi.org/10.1016/j.jweia.2024.105666

Deng, H., Ding, Y. S., Xiang, N. S., Xiang, T., Zhang, J., & Liang, X. F. (2024). Influence of covers for the bogies with external axle boxes on the aerodynamic drag of a high-speed train. *Journal of Railway Science and Engineering*, *21*(1), 26–37. https://doi.org/10.19713/j.cnki.43-1423/u.T20230209.

Dong, T. Y., Minelli, G., Wang, J. B., Liang, X. F., & Krajnovic, S. (2020). The effect of ground clearance on the aerodynamics of a generic high-speed train. *Journal of Fluids and Structures*, *95*, 102990. https://doi.org/10.1016/j.jfluidstructs.2020.102990

Du, H., Zhou, D., Meng, S., & Luo, C. Y. (2022). Effect of vortex generators on the aerodynamic performance of high-speed trains. *Flow, Turbulence and Combustion*, *109*(3), 627–645. https://doi.org/10.1007/s10494-022-00349-3

Gao, G., Li, J., He, F., Wang, K., Zhang, J. B., Miao, J., & J, X. (2019). Investigation of bogie positions on the aerodynamic drag and near wake structure of a high-speed train. *Journal of Wind Engineering and Industrial Aerodynamics*, *185*, 41–53. https://doi.org/10.1016/j.jweia.2018.10.012

Gritskevich, M. S., Garbaruk, A. V., Schutze, J., & Menter, F. R. (2012). Development of DDES and IDDES formulations for the k-ω shear stress transport model. *Flow, Turbulence and Combustion*, *88*(3), 431–449. https://doi.org/10.1007/s10494-011-9378-4

Guo, Z. J., Chen, X. D., Liu, T. H., Chen, Z. W., & Bordbar, A. (2024). Turbulence approaches for numerical predictions of vehicle-like afterbody vortex flows. *International Journal of Mechanical Sciences*, *283*, 109667. https://doi.org/10.1016/j.ijmecsci.2024.109667

Guo, J., Maryami, R., Yang, C. H., Yang, Y. N., Wang, X. N., & Liu, Y. (2023). Aerodynamic noise reduction of a blunt flat plate by trailing-edge blowing. *Physics of Fluids*, *35*(6), 065116. https://doi.org/10.1063/5.0154360

Huang, S., Hemida, H., & Yang, M. Z. (2016). Numerical calculation of the slipstream generated by a CRH2 high-speed train. *Proceedings of the Institution of Mechanical Engineers, Part F: Journal of Rail and Rapid Transit*, *230*(1), 103–116. https://doi.org/10.1177/0954409714528891

Huang, S., Zhang, B. D., Li, Z. W., Peng, W. J., & Lin, J. R. (2024). Aerodynamic characteristics of high-speed train pantographs based on jet flow control. *Journal of Applied Fluid Mechanics*, *17*(7), 1536–1551. https://doi.org/10.47176/jafm.17.7.1326

Jönsson, M., Wagner, C., & Loose, S. (2014). Particle image velocimetry of the underfloor flow for generic high-speed train models in a water towing tank. *Proceedings of the Institution of Mechanical Engineers, Part F: Journal of Rail and Rapid Transit*, *228*(2), 194–209. https://doi.org/10.1177/0954409712470607

Li, X. B., Liang, X. F., Wang, Z., Xiong, X. H., Chen, G., Yu, Y. Z., & Chen, C. M. (2021). On the correlation between aerodynamic drag and wake flow for a generic high-speed train. *Journal of Wind Engineering and Industrial Aerodynamics*, *215*, 104698. https://doi.org/10.1016/j.jweia.2021.104698

Li, T., Liang, H., Zhang, J., & Zhang, J. Y. (2023). Numerical study on aerodynamic resistance reduction of high-speed train using vortex generator. *Engineering Applications of Computational Fluid Mechanics*, *17*(1), e2153925. https://doi.org/10.1080/19942060.2022.2153925

Li, D. C., Meng, J. J., Bai, H., & Xu, R. X. (2018). Active control strategy for the running attitude of high-speed train under strong crosswind condition. *Vehicle System Dynamics, International Journal of Vehicle Mechanics and Mobility*, *56*(7), 1028–1050. https://doi.org/10.1080/00423114.2017.1403635

Li, T., Zhang, J., Rashidi, M. M., & Yu, M. (2019). On the reynolds-averaged navier-stokes modelling of the flow around aSimplified train in crosswinds. *Journal of Applied Fluid Mechanics*, *12*(2), 551–563. https://doi.org/10.29252/jafm.12.02.28958

Liang, X. F., Zhang, X., Chen, G., & Li, X. B. (2020). Effect of the ballast height on the slipstream and wake flow of high-speed train. *Journal of Wind Engineering and Industrial Aerodynamics*, *207*, 104404. https://doi.org/10.1016/j.jweia.2020.104404

Liu, N., Li, Y. S., Long, J. L., Jiang, C., He, L. F., Gao, G. J., & Miao, X. J. (2024). The study on the aerodynamic drag reduction of streamlined bogie and bottom deflector of high-speed train. *Journal of Railway Science and Engineering*, *21*(1), 38–47. https://doi.org/10.19713/j.cnki.43-1423/u.T20230238.

Melih, A., Kerem Tuğ, G., Ramazan, K., & Fazıl Selçuk, G. (2023). High fidelity CFD simulation of cavity flow and its active flow control using steady mass flow injection. *AIAA SciTech Form and exposition, American Institute of Aeronautics and Astronautics Inc, AIAA*. https://doi.org/10.2514/6.2023-0977.

Meng, S., Meng, S., Wu, F., Li, X. L., & Zhou, D. (2021). Comparative analysis of the slipstream of different nose lengths on two trains passing each other. *Journal of Wind Engineering and Industrial Aerodynamics*, *208*, 104457. https://doi.org/10.1016/j.jweia.2020.104457

Mitsumoji, T., Sato, Y., Ikeda, M., Sueki, T., & Fukagata, K. (2014). A basic study on aerodynamic noise reduction techniques for a pantograph head using plasma actuators. *Quarterly Report of RTRI (Railway Technical Research Institute)*, *55*(3), 184–189. https://doi.org/10.2219/rtriqr.55.184

Muñoz-Paniagua, J., & García, J. (2020). Aerodynamic drag optimization of a high-speed train. *Journal of Wind Engineering and Industrial Aerodynamics*, *204*, 104215. https://doi.org/10.1016/j.jweia.2020.104215

Niu, J. Q., Wang, Y. M., Liu, F., & Chen, Z. W. (2020). Comparative study on the effect of aerodynamic braking plates mounted at the inter-carriage region of a high-speed train with pantograph and air-conditioning unit for enhanced braking. *Journal of Wind Engineering and Industrial Aerodynamics*, *206*, 104360. https://doi.org/10.1016/j.jweia.2020.104360

Shur, M. L., Sparlart, P. R., Strelets, M. K., & Travin, A. K. (2008). A hybrid RANS-LES approach with delayed-DES and wall-modelled LES capabilities. *International Journal of Heat and Fluid Flow*, *29*(6), 1638–1649. https://doi.org/10.1016/j.ijheatfluidflow.2008.07.001

Sparlart, P., & Allmaras, S. (1992). *A one-equation turbulence model for aerodynamic flows. Technical report AIAA-92-0439*. American Institute of Aeronautics and Astronautics.

Thompson, D. J., Latorre lglesias, E., Liu, X. W., Zhu, J. Y., & Hu, Z. W. (2015). Recent developments in the prediction and control of aerodynamic noise from high-speed trains. *International Journal of Rail Transportation*, *3*(3), 119–150. https://doi.org/10.1080/23248378.2015.1052996

Wang, L. J., Alam, M. M., Rehman, S., & Zhou, Y. (2022). Effects of blowing and suction jets on the aerodynamic

performance of wind turbine airfoil. *Renewable Energy*, *196*, 52–64. https://doi.org/10.1016/j.renene.2022.06.126

Wang, S. B., Burton, D., Herbst, A., Sheridan, J., & Thompson, M. C. (2018). The effect of bogies on high-speed train slipstream and wake. *Journal of Fluids and Structures*, *83*, 471–489. https://doi.org/10.1016/j.jfluidstructs.2018.03.013

Wang, J. B., Gao, G. J., Li, X. B., Liang, X. F., & Zhang, J. (2019). Effect of bogie fairings on the flow behaviours and aerodynamic performance of a high-speed train. *Vehicle System Dynamics, International Journal of Vehicle Mechanics and Mobility*, *58*(6), 890–910. https://doi.org/10.1080/00423114.2019.1607400

Wang, J. B., Minelli, G., Dong, T. Y., He, K., Gao, G. J., & Krajnović, S. (2020). An IDDES investigation of Jacobs bogie effects on the slipstream and wake flow of a high-speed train. *Journal of Wind Engineering and Industrial Aerodynamics*, *202*, 104233. https://doi.org/10.1016/j.jweia.2020.104233

Xiao, C. H., Yang, M. Z., Tan, C. D., & Lu, Z. J. (2020). Effects of platform sinking height on the unsteady aerodynamic performance of high-speed train pantograph. *Journal of Wind Engineering and Industrial Aerodynamics*, *204*, 104284. https://doi.org/10.1016/j.jweia.2020.104284

Yao, S. B., Guo, D. L., Yang, G. W., & Li, M. G. (2012). Distribution of high-speed train aerodynamic drag. *Journal of the China Railway Society*, *34*(7), 18–23. https://doi.org/10.3969/j.issn.1001-8360.2012.07.003

Yousefi, K., & Saleh, R. (2014a). The effects of trailing edge blowing on aerodynamic characteristics of the NACA 0012 airfoil and optimization of the blowing slot geometry. *Journal of Theoretical and Applied Mechanics*, *52*(1), 165–179.

Yousefi, K., & Saleh, R. (2015). Three-dimensional suction flow control and suction jet length optimization of NACA 0012 wing. *Meccanica*, *50*(6), 1481–1494. https://doi.org/10.1007/s11012-015-0100-9

Yousefi, K., Saleh, R., & Zahedi, P. (2014b). Numerical study of blowing and suction slot geometry optimization on NACA 0012 airfoil. *Journal of Mechanical Science and Technology*, *28*(4), 1297–1310. https://doi.org/10.1007/s12206-014-0119-1

Zhang, J., Adamu, A., Gidado, F., Tang, M. Z., Ozer, O., & Chen, X. D. (2023a). Flow control for aerodynamic drag reduction of a high-speed train with diversion slots on bogie regions. *Physics of Fluids*, *35*(11), 115111. https://doi.org/10.1063/5.0172533

Zhang, J., Huang, F. Y., Yu, Y. Z., Han, S., Ding, Y. S., & Gao, G. J. (2023b). A novel wake flow control method for drag reduction of a high-speed train with vortex generators installing on streamlined tail nose. *Physics of Fluids*, *35*(10), 105139. https://doi.org/10.1063/5.0173350

Zhang, J., Wang, J. B., Wang, Q. X., Xiong, X. H., & Gao, G. J. (2018). A study of the influence of bogie cut outs' angles on the aerodynamic performance of a high-speed train. *Journal of Wind Engineering and Industrial Aerodynamics*, *175*, 153–168. https://doi.org/10.1016/j.jweia.2018.01.041

Zhang, J., Xu, A., Huang, F. Y., Bai, Y., & Liu, T. H. (2024). A novel vortex control method for improving anti-overturning performance of a high-speed train with leeward airbag structures under crosswinds. *Physics of Fluids*, *36*(6), 065146. https://doi.org/10.1063/5.0211370

Zhang, L., Yang, M. Z., & Liang, X. F. (2018). Experimental study on the effect of wind angles on pressure distribution of train streamlined zone and train aerodynamic forces. *Journal of Wind Engineering and Industrial Aerodynamics*, *174*, 330–343. https://doi.org/10.1016/j.jweia.2018.01.024

Zhu, J. Y., & Hu, Z. W. (2017). Flow between the train underbody and trackbed around the bogie area and its impact on ballast flight. *Journal of Wind Engineering and Industrial Aerodynamics*, *166*, 20–28. https://doi.org/10.1016/j.jweia.2017.03.009